

UNIVERSIDAD DE SANTIAGO DE COMPOSTELA



FACULTAD DE FÍSICA  
Departamento de Física de Partículas

**Conceptual Design of a Large Area  
Time-of-Flight Wall for the R<sup>3</sup>B experiment  
at FAIR**

Memoria presentada por:  
**David Pérez Loureiro**  
como disertación para optar al  
**Grado de Licenciado en Física**  
Junio 2005



# UNIVERSIDAD DE SANTIAGO DE COMPOSTELA

José Benlliure Anaya, Profesor Titular de Física Atómica, Molecular y Nuclear de la Universidad de Santiago de Compostela,

Ignacio Durán Escribano, Catedrático de Física Atómica, Molecular y Nuclear de la Universidad de Santiago de Compostela,

**CERTIFICAN:** que la memoria titulada **Conceptual Design of a Large Area Time-of-Flight wall for the R<sup>3</sup>B experiment at FAIR** ha sido realizada por **David Pérez Loureiro** en el **Departamento de Física de Partículas de esta Universidad** bajo nuestra dirección y constituye el trabajo de **tesina** que presenta para optar al **Grado de Licenciado en Física**.

Santiago, 15 de Junio de 2005

Fdo: José Benlliure Anaya

Fdo: Ignacio Durán Escribano



*A mis padres  
y hermana.*



# Contents

<b>Introduction</b>	<b>1</b>
<b>1 The R<sup>3</sup>B experiment</b>	<b>5</b>
1.1 Physics program at the <i>R<sup>3</sup>B</i> experiment . . . . .	5
1.2 Layout of the experiment . . . . .	6
1.2.1 $\gamma$ -ray detection . . . . .	7
1.2.2 Neutron detection . . . . .	8
1.2.3 Light charged particles and ion detection . . . . .	8
1.3 Detector requirements for isotopic identification . . . . .	10
1.3.1 Charge and mass resolution . . . . .	10
1.3.2 Magnetic rigidity and time-of-flight resolution . . . . .	10
1.3.3 Size of the ToF detector . . . . .	12
1.3.4 Segmentation of the detector . . . . .	14
1.4 Physical limitations to the velocity resolution . . . . .	16
1.5 Proposed requirements for the ToF wall detector . . . . .	17
<b>2 Time-of-Flight detectors.</b>	<b>19</b>
2.1 Resistive plate chambers (RPCs) . . . . .	19
2.1.1 Fundamentals of resistive plate chambers . . . . .	19
2.1.2 Performances of RPCs . . . . .	22
2.2 Scintillation detectors . . . . .	27
2.2.1 General features . . . . .	27
2.2.2 Organic scintillator materials . . . . .	28
2.2.3 Performances of scintillation detectors . . . . .	29
2.3 Summary and conclusions . . . . .	31
<b>3 Performance test of Read-out electronics</b>	<b>33</b>
3.1 Standard modular electronics . . . . .	33
3.1.1 Experimental Setup . . . . .	33
3.1.2 Results . . . . .	34
3.2 Signal digitation and pulse shape analysis . . . . .	35

3.2.1	Experimental Setup . . . . .	36
3.2.2	Analysis software (PIFFIA) . . . . .	37
3.2.3	Results . . . . .	41
3.3	FEE+TAQUILA digitation card . . . . .	47
3.3.1	Experimental Setup . . . . .	47
3.3.2	Results . . . . .	49
3.4	Conclusions . . . . .	50
<b>4</b>	<b>Conceptual Design</b>	<b>53</b>
4.1	Design concepts . . . . .	53
4.1.1	RPCs . . . . .	53
4.1.2	Plastic scintillators . . . . .	58
4.2	Cost estimate . . . . .	59
4.2.1	RPCs . . . . .	59
4.2.2	Plastic scintillators . . . . .	60
	<b>Conclusions</b>	<b>63</b>
	<b>Conclusiones</b>	<b>67</b>
<b>A</b>	<b>Bending angle and position resolution</b>	<b>71</b>
<b>B</b>	<b>Simulation codes</b>	<b>73</b>
B.1	Estimation of multihit probability in fission . . . . .	73
B.2	Multifragmentation . . . . .	76
	<b>Agradecimientos</b>	<b>85</b>

# Introduction

Atomic nucleus is a quantum system with a finite number of strongly interacting fermions: protons and neutrons. Interaction between nucleons cannot be treated in a perturbative way because of the large value of the coupling constant. It is also not possible to treat nucleons statistically, due to the fact that the number of them is not large enough. Furthermore, electromagnetic and weak interaction are also present in the nucleus. By using bare nucleon-nucleon interaction as starting point, it has been possible to describe light nuclei up to mass 10 based on first principles. Going to heavier nuclei, the interactions are modified by the medium and effective interactions are needed. Nuclear mean fields can be generated in a self-consistent way by using effective two-body nucleon-nucleon forces. The nuclear shell model starts from a different basis by dividing the nucleus into an inert core and a number of valence nucleons. New techniques and increased computer power have resulted in the last decade to the description of medium-heavy nuclei.

Most of the present day knowledge of the structure of the atomic nucleus is based on the properties of nuclei close to the line of  $\beta$ -stability where the proton-to-neutron ratio is not so different to that of stable nuclei. But extrapolating this to the region far from stability is quite dangerous and some of the ‘basic truths’ of nuclear physics have to be revisited. For instance, the nuclear radii of some nuclei do not scale with the mass as  $A^{1/3}$ . Also, the well known magic numbers for  $Z$  and  $N$  seem to be dependent on  $N$  and  $Z$ , respectively. The dependence of the nuclear interaction on the proton-to-neutron ratio (expressed by the quantum number isospin), is believed to provide better knowledge on some aspects of the nuclear interaction and dynamics. The study of nuclei under extreme conditions of isospin will not only provide firm guidance for theoretical models, but also it leads to the discovery of new phenomena. Such nuclei, far off stability are called ‘exotic’.

During the last decade it has been demonstrated that reactions with high energy secondary beams are an important tool to explore properties of nuclei far off stability, which allows to extract detailed spectroscopic information. Secondary beam technique, consisting on accelerating radioactive nuclei cre-

ated on a previous reaction, allows to produce very exotic nuclear species varying in a wide range in proton-neutron ratios which do not exist in nature. The isotopes produced by this method can be used in two different ways:

- by stopping them, some information of the energy levels can be extracted with different methods, such as  $\beta$ -delayed  $\gamma$  spectroscopy and isomer spectroscopy.
- they can also be used to undergo nuclear reactions in secondary targets in order to study the reaction dynamics with these exotic species.

While the field of ‘radioactive ion beams’ (RIB), is linked mainly to the study of nuclear structure under extreme conditions of isospin, mass, spin and temperature, it also addresses problems in nuclear astrophysics, solid state physics and the study of fundamental interactions.

Radioactive beams have been developed in a number of European Large-Scale Facilities. Pionering experiments and strong development programmes are ongoing in Europe, North america and Japan on existing facilities. In addition a new generation of large scale RIB facilities is being built. The FAIR project is one of them [1].

FAIR (Facility for Antiproton and Ion Research) is an international accelerator facility of the next generation (Fig. 1). It builds on the experience and technological developments already made at the existing GSI facility, and incorporates new technological concepts. At its heart is a double ring facility with five times the circumference of the current heavy ion synchrotron (SIS). A system of cooler-storage rings for effective beam cooling at high energies and various experimental halls will be connected to the facility.

The existing GSI accelerators serve as injector for the new facility. The double-ring synchrotron will provide ion beams of unprecedented intensities as well as of considerably increased energy. Thereby, intense beams of secondary beams –unstable nuclei or antiprotons– can be produced. The system of storage-cooler rings allows the quality of these secondary beams – their energy spread and emittance– to be drastically improved. Moreover, in connection with the double ring synchrotron, an efficient parallel operation of up to four scientific programs can be realized at a time.

One of the experiments which will take place in this new facility is  $R^3B$  (Reactions studies with Relativistic Radioactive Beams). The aim of this project is the design and the implementation of an advanced experimental facility for studies with exotic nuclei by means of reactions with secondary beams at relativistic energies.

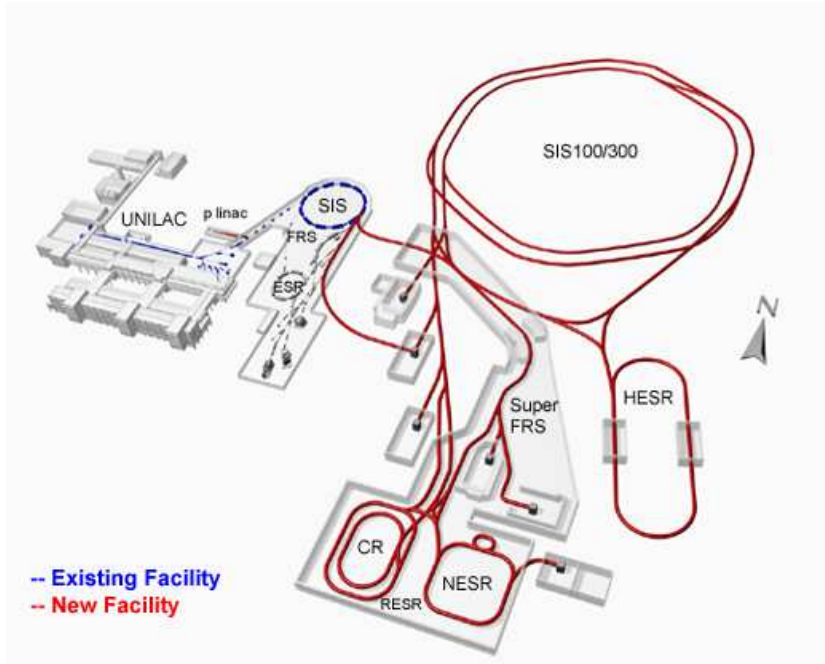


Figure 1: Schematic picture of the FAIR facility. In blue are shown the GSI existing facilities. In red are shown the new accelerator and the new experimental areas.  $R^3B$  will be placed downstream the Super-FRS

The technical challenge of this project is to detect and fully identify in mass and charge and to determine the momenta of all the outgoing products from the reactions induced by exotic nuclei. To achieve this aim, a complex system of detection devices has been proposed. The measurement of the energy loss of the reaction products by ionization chambers allows the determination of the atomic number. This, combined with the use of strong magnetic fields for determining the magnetic rigidity, together with a determination of the velocity, will provide the mass number.

One of the possibilities considered for the velocity measurement is the use of a Time-of-Flight (ToF) detector. Most of the detectors of this kind used until now for the identification of heavy ions were based on plastic scintillators coupled to photomultiplier tubes. However, the very successful developments in resistive plate chambers (RPCs), excellent time resolutions and efficiencies close to 100 % have been achieved for MIPs. This fact, together with the lower cost per electronics channel compared with scintillator technology, make this type of detectors a very encouraging alternative for velocity determination with heavy ions.

The goal of this work is to define the performances of the ToF wall de-

detector in order to satisfy the requirements (full acceptance and good time resolution), investigate the possible present technologies to achieve this aim and propose a conceptual design based on the previous considerations. The two possible technologies mentioned before have been considered: the use of fast scintillators coupled to ultra-fast phototubes and RPCs. In order to analyze and discuss this two possibilities, we will divide the work in four different chapters.

- In the first chapter, an overview to the  $R^3B$  project is presented, the experimental setup and the detectors are described, as well as the experimental method for the identification. We also discuss the detector requirements (time resolution, size and granularity).
- In the second chapter, the two most extended technologies for time-of-flight measurements, RPCs and plastic scintillators, are discussed. The performances of these two technologies in recent experiments are also described.
- In the third chapter, a performance test of different readout methods for fast detectors is presented. These methods are the use of standard electronics (TAC and ADC), complete digitation of the signal combined with later software analysis and the use of a complete new fast electronics developed at GSI for the FOPI experiment [2].
- In the fourth chapter, a conceptual design for the construction of an RPC based Time-of-Flight wall which fulfills all the requirements is given.

# Chapter 1

## The $R^3B$ experiment

The goals of the  $R^3B$  project are to design and implement an advanced experimental setup for Reaction studies with Relativistic Radioactive ion Beams. The experiments will take place at the focal plane of the high energy branch of the Super FRS at the new FAIR facility in Darmstadt (Germany). The energies of the ion beams will be between 0.5 and 1 GeV per nucleon.

$R^3B$  will provide unique experimental conditions worldwide for experiments with relativistic secondary beams in order to benefit researchers in the fields of nuclear structure physics, nuclear reaction physics and nuclear astrophysics.

### 1.1 Physics program at the $R^3B$ experiment

The different reaction types and associated physics goals that can be achieved at the  $R^3B$  experimental setup are described in this section.

**Total-absorption measurements.** Nuclear *matter radii* may be inferred from total interaction cross sections derived from total-absorption measurements of radioactive ions in thick targets. These data together with isotope shift measurements, provide a first experimental manifestation of *neutron skins* [3].

**Elastic-proton scattering.** The radial distribution of *nuclear density* of exotic nuclei may be extracted from high energy proton elastic scattering. Previous experiments have demonstrated the power of the method to investigate *halos* and *skins* in nuclei far off stability [4].

**Knockout reactions.** Break-up reactions induced by high-energy beams of exotic nuclei allow the exploration of *ground-state* configurations and

of excited states. Knockout reactions have been used in particular to map the halo nucleon wave function in momentum space, from which their spatial distribution is derived via Fourier transformation [5].

**Quasi-free scattering.**  $R^3B$  experiment intends to develop and apply the technique of quasi-free scattering using radioactive beams in inverse kinematics. This type of reactions allows to extract information of the *single-particle shell-structure*, *nucleon-nucleon correlations* as well as *cluster* knockout reactions [6].

**Electromagnetic excitation.** Electromagnetic processes in heavy ion interactions at energies far above the Coulomb barrier give access to a wealth of nuclear structure information on exotic nuclei. *Surface vibrations* and *giant resonances* can be studied [7].

**Charge exchange reactions.** The (p,n) charge exchange reaction can be used to excite Gamow Teller (GT) and spin dipole resonances. Studies of the GT strength are beside their importance in nuclear structure of particular astrophysical interest. Electron-capture reactions leading to stellar collapse and supernova formation are mediated by GT transitions [8].

**Fission.** Since fission corresponds to a typical large-scale motion process, it has been recognised as one of the most promising tools for deducing information on *nuclear viscosity*, and on *shell effects* and *collective excitations at extreme deformation* [9].

**Spallation reactions.** Spallation reactions are important in various fields of research such as *astrophysics*, *neutron sources* and *production of radioactive beams* [10].

**Projectile fragmentation & multifragmentation.** Heavy ions collisions offer the possibility to probe nuclear matter under extreme conditions of densities and temperatures. Isotopic effects in multifragmentation, reflect the strength of the symmetry term in the *equation of state*. Projectile fragmentation of secondary beams in conjunction with  $\gamma$ -ray spectroscopy is a powerful method to explore *excited states in exotic nuclei* [11].

## 1.2 Layout of the experiment

For a complete kinematic measurement, all the particles coming out from the nuclear reaction have to be identified in mass and charge. Their momenta

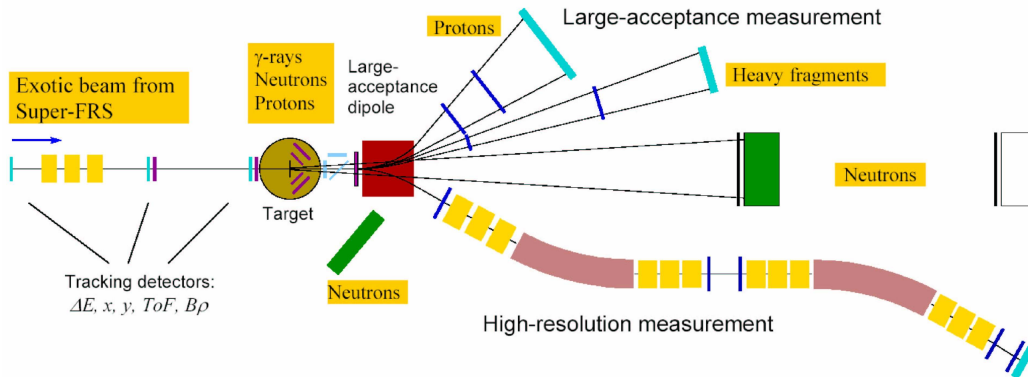


Figure 1.1: Schematic picture of the  $R^3B$  experimental setup. From left to right, we can see the secondary target, the  $\gamma$ -detector, the large acceptance superconducting dipole magnet, three position detectors for tracking, the neutron detector (LAND), and a ToF wall for charged particles identification. At the bottom of the picture, the high resolution magnetic spectrometer for the high resolution mode is shown.

have to be also measured very accurately. The proposed experimental setup is described in the following (Fig. 1.1).

Two modes of operation are foreseen depending on the demands of the experiments:

**Large acceptance mode:** Heavy fragments and light charged particles are deflected by a large acceptance dipole and detected with full solid-angle acceptance.

**High resolution mode:** Here, the dipole magnet is operated in reversed mode, deflecting the fragments into a high resolution magnetic spectrometer.

The large gap of the dipole provides a free cone for the neutrons, which are detected in forward direction by the Large Area Neutron Detector (new LAND).

The  $R^3B$  proposal also includes the measurement of the emitted gamma rays with a  $4\pi$   $\gamma$ -calorimeter around the target.

### 1.2.1 $\gamma$ -ray detection

This detector should have high efficiency and good angular resolution. It should also have a high absorption probability for photons with energies up

to 10 MeV, due to the Lorentz boost of the  $\gamma$ -photons emitted. Besides the  $\gamma$ -sum, the calorimeter has to provide the  $\gamma$ -multiplicity and the individual  $\gamma$ -energies for spectroscopic purposes. Two design possibilities have been taken into account. Either an array consisting on cooled scintillators (such as CsI or NaI) or new inorganic scintillator materials, like LaBr<sub>3</sub>. The light read-out will be performed by PIN diodes.

### 1.2.2 Neutron detection

The Large Area Neutron Detector has been designed for the detection of high energy neutrons and determine their momenta via Time-of-Flight and position measurement. An efficiency of more than 90% for 400 MeV neutrons and a time resolution in the order of 100 ps are required. Two possible technologies have been considered in its design, either a sandwich of iron converters and plastic scintillator or Resistive Plate Chambers (RPCs).

### 1.2.3 Light charged particles and ion detection

#### Atomic number determination

The measurement of the atomic number  $Z$  can be done with a Multi Sampling Ionization Chamber (MUSIC), which consists on an ionization chamber whose anode is segmented in several anode plates in order to achieve a better resolution in charge determination [12].

#### Mass number determination

For the charged particles (e.g. protons and ions), the measurement of the magnetic rigidity, together with the velocity, makes possible their identification in mass-over-charge ratio ( $A/Q$ ) according to the following equation:

$$B\rho = \frac{931.5}{c} \gamma\beta \frac{A}{Q} \quad (1.1)$$

where  $B\rho$  is the magnetic rigidity,  $\gamma$  is the Lorentz factor and  $\beta$  is the velocity of the ion. For measuring the  $B\rho$ , two different elements are needed: a large acceptance dipole magnet, and a set of tracking detectors.

The characteristics of the different detectors are described in the the following.

**Dipole magnet.** This superconducting dipole magnet has the following parameters: a large vertical gap providing an angular acceptance of  $\pm 80$

mrاد for neutrons, a maximum bending angle of  $40^\circ$ , ensuring an acceptance close to 100% and a high field integral of about 5 Tm, which allows a bending angle of  $18^\circ$  for a 15 Tm beam.

**Tracking detectors.** Three tracking detectors are needed in order to reconstruct the trajectory of any particle through the dipole and determine their bending angle. One of these detectors will be placed in front of the dipole and the other two behind the magnet. These detectors should provide a position resolution of  $200\ \mu\text{m}$ . Different types of detectors such as a Time Projection Chamber (TPC), multiwire chambers or scintillating fibers are being considered as tracking detectors.

### Velocity measurement

For the measurement of the velocity two methods could be used, Time-of-Flight (ToF) or a Ring Imaging Cherenkov (RICH) detector.

The RICH detector is based on the phenomenon known as *Cherenkov radiation emission*. This effect consists on the emission of photons when a particle traverses a medium with a velocity higher than the speed of light in that medium. The Cherenkov detector provides a resolution of  $10^{-3}$ . However, the thickness of the radiator, the medium which produces the Cherenkov light, represents a substantial target in the beam and we can not distinguish between the reactions produced in the target and in the radiator. The reaction probability of medium-mass nuclei at 600 MeV/u impinging a  $\text{MgF}_2$  radiator (2 mm thickness) is around 7% [13].

In ToF technique, the time between two points separated a known distance  $d$ , is measured. Velocity is then calculated as  $v = \frac{d}{T_{oF}}$ . From eq. (1.1), one can obtain mass over charge ratio combining the  $B\rho$  and velocity measurement.

This method of determining the velocity needs two time detectors, one which acts as a START detector and another one which gives the STOP. The total Time-of-Flight resolution will be determined by the quadratic sum of START and STOP resolutions ( $\sigma_{START}$  and  $\sigma_{STOP}$ ).

$$\sigma_{ToF} = \sqrt{\sigma_{START}^2 + \sigma_{STOP}^2} \quad (1.2)$$

In the  $R^3B$  project, two different types of detectors are proposed. The START will be given by a CVD (Chemical Vapor Deposition) diamond detector. Diamond is an insulator, but due to the fact that it contains defects and impurities, it behaves like a semiconductor, which makes it useful for several electronic applications. Compared to Silicon, the main advantages of

diamond are a higher electron mobility and thus a fast signal, a high resistivity which leads to a small leakage current ( $\sim$  few pA). But on the other hand, the number of electrons created by a charged particle is smaller in diamond than in Silicon (36 against 89 per micron). The typical size of this type of detectors is of few  $\text{cm}^2$  and a thickness of hundreds of  $\mu\text{m}$ . The intrinsic time resolution is 29 ps ( $\sigma$ ) [14].

The STOP signal will be provided by a large area Time-of-Flight wall, based either on scintillators coupled to ultra fast photomultiplier tubes or on resistive plate chambers. The requirements of such a detector are described in the next section.

### 1.3 Detector requirements for isotopic identification

As it was mentioned before, in order to perform a complete kinematic measurement of the reactions, all the particles created have to be completely identified (charge, mass, and momentum).

#### 1.3.1 Charge and mass resolution

To identify the atomic number of the reaction products up to  $Z=92$ , one needs a relative resolution in charge of  $\Delta Z/Z \sim 0.5 \times 10^{-2}$ . This resolution is easily reached with a MUSIC, which provides an accuracy of 0.3 charge units for ions below  $Z = 80$  [15]. In  $R^3B$  experiment the MUSIC will be placed between the two last tracking detectors.

Once we have determined the atomic number, we need to separate the different isotopes of a certain element. In order to be able to solve two neighboring nuclei around the mass 200, a resolution in mass-to-charge ratio  $\Delta(A/Q)/(A/Q) \sim 2.25 \times 10^{-3}$  is required.

#### 1.3.2 Magnetic rigidity and time-of-flight resolution

From eq. (1.1), one obtains:

$$\begin{aligned} \left( \frac{\Delta(A/Q)}{A/Q} \right)^2 &= \frac{1}{(A/Q)^2} \left[ \left( \frac{\partial(A/Q)}{\partial(B\rho)} \right)^2 (\Delta(B\rho))^2 + \left( \frac{\partial(A/Q)}{\partial\beta} \right)^2 (\Delta\beta)^2 \right] \\ &= \left( \frac{\Delta(B\rho)}{B\rho} \right)^2 + \frac{1}{(1-\beta^2)^2} \left( \frac{\Delta\beta}{\beta} \right)^2 \end{aligned} \quad (1.3)$$

This expression can be written in a different way by using the relation between  $\beta$  and  $ToF$ .

$$\left(\frac{\Delta(A/Q)}{A/Q}\right)^2 = \left(\frac{\Delta(B\rho)}{B\rho}\right)^2 + \frac{ToF^4 c^4}{((ToFc)^2 - d^2)^2} \left(\frac{\Delta(ToF)}{ToF}\right)^2 \quad (1.4)$$

The accuracy in the determination of the magnetic rigidity,  $B\rho$ , is given by the accuracy in the measurement of the bending angle,  $\theta$  induced by the large dipole magnet.

$$\frac{\Delta\theta}{\theta} = \frac{\Delta(B\rho)}{B\rho} \quad (1.5)$$

This value is related to the resolution of the tracking detectors and the maximum magnetic field of the dipole.

$$\Delta\theta = \frac{\sqrt{(\Delta x_1)^2 + (3\Delta x_2)^2 + (2\Delta x_3)^2}}{\ell} \quad (1.6)$$

where  $\Delta x_i$  are the position resolution of the tracking detectors and  $\ell$  is the distance between them.  $\Delta x_2$  has to take into account the angular straggling in position detector 1. The straggling in the position detector 2 and the ionization chamber has to be included in  $\Delta x_3$ . A detailed derivation of eq. (1.6) is shown in appendix A.

The resolution of the tracking detectors is assumed to be  $200 \mu\text{m}$ . The straggling induced by the position detectors considering a distance around 1.2 m between them is 0.19 mrad and 0.38 mrad for the MUSIC, this values have been calculated by using AMADEUS code [16], which allows to simulate the interaction of relativistic heavy ions with matter. From eq. (1.6) we obtain the value of the accuracy in the measurement of the bending angle  $\theta$  for  $\ell = 1.2$  m.

$$\Delta\theta = 0.67 \text{ mrad}$$

If we want to separate a fission fragment with atomic number  $Z = 64$  and mass around  $A = 160$  at 600 MeV/u ( $B\rho = 10.137$ ), the bending angle<sup>1</sup> is  $\theta = 226.24$  mrad. This means that the resolution in magnetic rigidity, should be  $\frac{\Delta B\rho}{B\rho} = 2.96 \times 10^{-3}$ . In order to achieve the required resolution  $\Delta A/A \sim 0.5/160$  the time of flight should be determined with an accuracy around  $10^{-3}$ . The time resolution required for mass  $A = 200$  is slightly high ( $7 \times 10^{-4}$ ) and depending on the distance between start and stop detectors (path-length,  $d$ ), the absolute resolution needed will take different values, as shown in figure 1.2. As we can see the required resolution increases with the mass of the nucleus we want to separate. For a 15 m pathlength, the

---

<sup>1</sup>The dipole magnet is designed to provide  $18^\circ$  for a 15 Tm beam

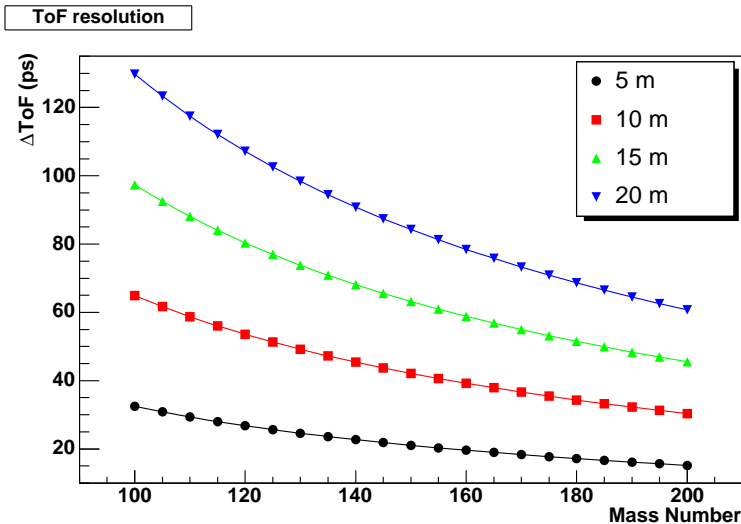


Figure 1.2: Time of flight resolution needed to solve two neighbouring fragments at 700 MeV/u for different flight path-lengths and masses.

resolution needed to separate neighbouring isotopes, is ranging from 45.5 ps of  $A = 200$  to 95 ps of  $A = 100$  (FWHM). This results allow us to consider this distance as the most appropriate, due to the fact that the time resolution needed is achievable by using present technology. Time resolutions required for shorter distances represents a challenge ( $\sigma_{ToF} \approx 10.9$  ps for  $A = 200$ ). For longer distances, the size of the detector makes too big, as shown in next subsection.

### 1.3.3 Size of the ToF detector

At first glance, the larger the path-length, the lower the time resolution needed, but we have to take into account other requirements. One of them is the size of the STOP detector. The main requirement is to cover the full acceptance of the fragments produced in collisions induced by relativistic heavy ions. In order to estimate the size of the detector that fulfils the condition, we are going to consider the reaction mechanism that covers the larger angular range, fission.

Let us consider a  $^{238}\text{U}$  nucleus at 500 MeV/u which fissions in two fragments of charges  $Z_1 = 20$  and  $Z_2 = 72$  respectively. By using Wilkins model [17], we can obtain the value of the total kinetic energy available in the center

of mass frame.

$$TKE = \frac{Z_1 Z_2 e^2}{D} \quad (1.7)$$

$$D = r_0 A_1^{1/3} \left(1 + \frac{2}{3} \beta_1\right) + r_0 A_2^{1/3} \left(1 + \frac{2}{3} \beta_2\right) + d \quad (1.8)$$

where  $Z_1, Z_2, A_1$  and  $A_2$  are the atomic numbers and the masses of the fission fragments respectively.  $\beta_1 = 0.6$  and  $\beta_2 = 0.6$  are the deformation coefficients.  $r_0 = 1.16$  fm,  $d = 2$  fm.

By using momentum and energy conservation laws, the velocity of the fragments in center of mass frame can be obtained as.

$$v_1^{cm} = \sqrt{\frac{2A_2 TKE}{A_1(A_1 + A_2)}} \quad v_2^{cm} = \frac{A_1}{A_2} v_1^{cm} \quad (1.9)$$

Once we have the modules of the velocities, the different space coordinates are

$$v_x^1 = v_1^{cm} \sin \theta \cos \phi \quad v_x^2 = v_2^{cm} \sin \theta \sin \phi \quad (1.10)$$

$$v_y^1 = v_1^{cm} \cos \theta \quad v_y^2 = v_2^{cm} \sin(\pi - \theta) \cos \phi \quad (1.11)$$

$$v_z^1 = v_1^{cm} \sin(\pi - \theta) \sin \phi \quad v_z^2 = v_2^{cm} \cos(\pi - \theta) \quad (1.12)$$

where  $\theta$  and  $\phi$  are the polar and azimuthal angles in spherical coordinates. Due to the fact that the distribution is isotropic, in order to simplify the calculations, we can take  $\phi = 0^\circ$ .  $\theta$  is also fixed to  $90^\circ$  because is the angle which will give the maximum angular aperture after a Lorentz transformation.

A boost in the beam direction ( $z$  axis), will transform the velocities to the laboratory frame.

$$v_x^{LAB} = \frac{v_x^{cm}}{\gamma \left(1 + \frac{\vec{v} \cdot \vec{\beta}}{c}\right)} \quad v_z^{LAB} = \frac{\beta c}{\left(1 + \frac{\vec{v} \cdot \vec{\beta}}{c}\right)} \quad (1.13)$$

The angle between the velocity vector and the beam line can be calculated as

$$\theta^{LAB} = \arctan \left( \frac{v_x^{LAB}}{v_z^{LAB}} \right) \quad (1.14)$$

With this simple calculation, one can estimate the size of the detector. The fragments produced by fissioning  $^{238}\text{U}$  nuclei at 500 MeV/u, will be emitted with a maximum angle in the laboratory frame of  $\theta^{LAB} \approx 53.4$

$d$ (m)	$size(m)$
5	0.54
10	1.07
15	1.60
20	2.13

Table 1.1: Size needed of the detector to cover the full acceptance of the fission fragments.

mrاد. The sizes which correspond to different path-lengths are presented in table 1.1. As one can see, in order to cover the full acceptance of fission fragments at 500 MeV/u, for 15 m the size of the detector required is  $1.5 \times 1.5$  m<sup>2</sup>, therefore the full acceptance for larger energies is guaranteed due the the larger forward focusing produced by Lorentz boost.

### 1.3.4 Segmentation of the detector

Another requirement of the detector is to minimize the multihit probability, that in the case of fission, occurs when both fission fragments hit the same strip of the detector. This factor is also important because of the number of electronics channels needed. It is clear that the smaller the strips, the lower multihit probability, but the larger the number of channels needed to cover the full size of the detector.

For the estimation of the multihit probability, a simple simulation program has been developed. The code is shown in appendix B.

The simulation consists on the following:  $^{238}\text{U}$  nuclei fission or break into three or five fragments isotropically in the center of mass frame. Reaction products are Lorentz boosted. Positions of fission products or fragments ( $x, y$ ) are calculated in a perpendicular plane to the beam axis situated 15 m downstream. (Figure 1.3)

Assuming the strips are paralell to  $x$  and  $y$  axes, by calculating the difference of the  $x$  and  $y$  coordinates of all the fragments, one can know whether they have hit the same strip of the detector or not. The ratio between the number of multihit events and the number of simulated uranium nuclei, gives the probability of multihit, provided this number is large enough. The values obtained for different sizes of the strips are shown in figure 1.4. As we can see, the probability of multihit increases with the size of the strip and the

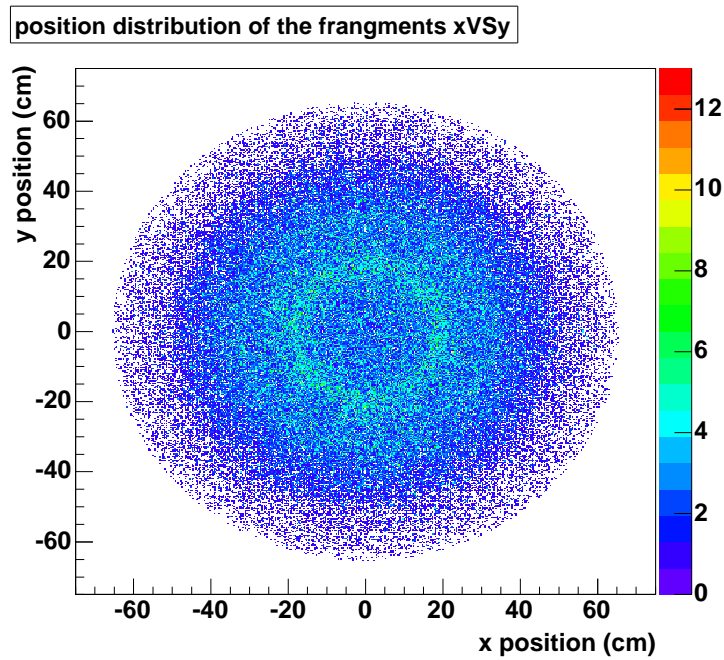


Figure 1.3: Distribution of position of the fission fragments in the STOP detector at 15 m downstream.

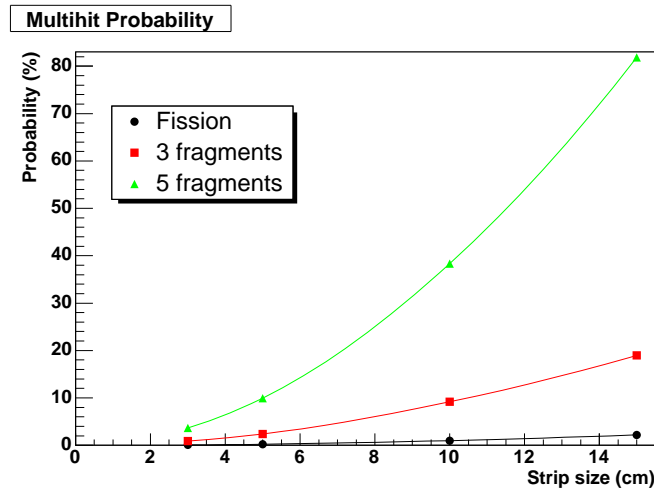


Figure 1.4: Probability of Double hit for different sizes of the strips of the detector for 15 m pathlength. As we can see, a strip size of 5 cm, gives probabilities lower than 10% for fission and multifragmentation reactions.

multiplicity of the events. For 5 cm strips, the probability of double hit is lower than 10 % in all cases, reaching less than 1% for the fission. Therefore,

this strip size seems the most appropriate. Smaller strips would require too much electronic channels.

## 1.4 Physical limitations to the velocity resolution

In order to correct the velocity measurement due to different path-lengths of the reaction products, one has to determine the impact position in the ToF wall. This can be done by measuring the time at both sides of a given strip. As it will be shown, the position resolution will be limited by the time resolution. Let us consider a strip of length  $L$  and let us assume a particle hitting the detector in a position  $x$  (see figure 1.5). The time values at both sides of the strip will be:

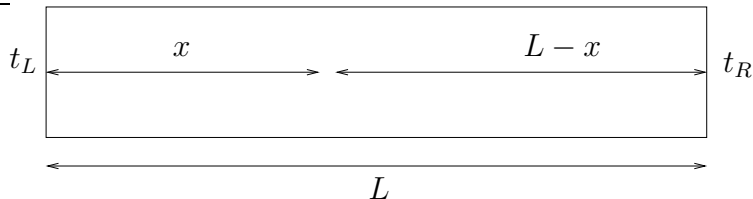


Figure 1.5: Strip of the detector hit by a particle at a certain position  $x$ .

$$t_L = t_0 + \frac{x}{v_p} \quad (1.15)$$

$$t_R = t_0 + \frac{L - x}{v_p} \quad (1.16)$$

where  $t_L$  and  $t_R$  are the left and right times,  $t_0$  is the real time-of-flight, and  $v_p$  is the propagation velocity of the signal within the detector. By subtracting eqs. (1.15) and (1.16), one can obtain the relation between the time difference and the position.

$$\Delta t = t_L - t_R = \frac{2x - L}{v_p} \quad (1.17)$$

From equation (1.17), we obtain:

$$\delta(\Delta t) = \frac{2}{v_p} \delta x \quad (1.18)$$

This equation relates the time resolution with the position accuracy. The propagation velocity depends on the detection device used. For instance,

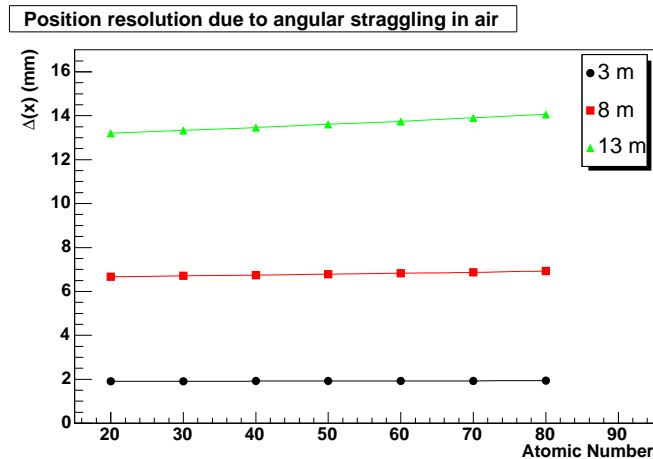


Figure 1.6: Position resolution due to angular straggling for different lengths of flight path.

$v_p = 18.92$  cm/ns for plastic scintillators (Bicron BC420) while for RPCs is 13.41 cm/ns ( $v_p = c/n$ , where  $n$  is the refraction index), thus we can calculate the position resolution achieved with the time required resolution ( $\sigma \sim 20$  ps for  $A=200$ ). From (1.18), we obtain  $\delta x = 1.9$  mm for the scintillator and 1.3 mm for an RPC.

If the impact position in the ToF detector is not measured by the left-right time difference, the resolution in the position at the ToF wall will be given by the angular straggling in the air from the last tracking detector to the STOP detector. Figure 1.6, shows the position resolution due to the angular straggling for atomic numbers from 20 to 80 and different distances between the last tracking and the ToF wall. As we can see, for 8 m, the position resolution is not better than 7.3 mm. The measurement of the position by the left-right differences at the ToF wall, improves the resolution to 2 mm or better, therefore the accuracy in the determination of the velocity will not be limited by the position resolution, thus the addition of a tracking detector is not needed.

## 1.5 Proposed requirements for the ToF wall detector

According to the results obtained in the previous section for time resolution, size of the detector, and low multihit probability for fission and multifragmentation reactions, the most appropriate characteristics are described

in the following.

The ToF wall should be placed around 15 m downstream from the target. The angular straggling produced by 8 m of air from the last tracking detector to the ToF wall will not limit the velocity resolution required. The resolution achieved in the position from left-right time differences is lower than 2 mm. The time accuracy needed to separate masses around  $A \sim 200$  at 700 MeV/u for 15 m pathlength is  $\sigma_{ToF} \approx 20$  ps. Due to the fact that diamond detectors' intrinsic time resolution is  $\sigma = 29$  ps, the resolution will be limited by this value. Other possible detectors should be considered as START in order to avoid this limitation. As far as size is concerned, the one required to cover the full acceptance for fission fragments is  $1.5 \times 1.5$  m<sup>2</sup>. The detector will be divided in strips of 5 cm, providing a multihit probability lower than 10% for multifragmentation reactions (5 fragments).

Two different technologies can be used to implement such a detector: Resistive Plate Chambers (RPC), or fast plastic scintillators attached to fast photomultiplier tubes. Both methods will be explained in detail in the next chapter.

# Chapter 2

## Time-of-Flight detectors.

In this chapter, two different kinds of detectors for the  $R^3B$  large area ToF wall are presented, organic scintillators coupled to fast photomultiplier tubes (PMTs), and resistive plate chambers (RPCs). Both technologies are the most extended nowadays for time-of-flight measurements. Here we will present both types of detectors and we will discuss their performances for ToF measurements.

### 2.1 Resistive plate chambers (RPCs)

These detectors were introduced in 1981 [18] as a practical alternative to the remarkable ‘localized discharge spark counters’ developed by Pestov [19], which provides a very good time resolution ( $\sigma \sim 25$  ps). Their main difference is that RPCs work at atmospheric pressure, while the Pestov counter requires higher pressures. Another drawback of the Pestov detectors is the fact that the gas mixture used is flammable.

#### 2.1.1 Fundamentals of resistive plate chambers

RPCs are gaseous detectors with a uniform electric field produced by two parallel electrode plates, one of which —at least— is made of a material with high bulk resistivity. The gap between the two electrodes, ranging from a few hundred micron to millimeters, depending on the application, is filled with a gas mixture with a high absorption coefficient for ultraviolet photons and very good electron affinity. The electrons and the ions created by the incoming particle are accelerated towards the anode and the cathode, respectively. When the primary ionization gains enough energy to ionize other gas molecules, secondary electrons are created. This new electrons can

produce new ionizations, leading to the formation of an avalanche. The total number of electrons created in a path  $x$ , is [20]:

$$n = n_0 \exp(\alpha x) \quad (2.1)$$

where  $n_0$  is the initial number of electrons and  $\alpha$  is the first Townsend coefficient. The factor  $e^{\alpha x}$ , known as multiplication factor, is limited to about  $10^8$  or  $\alpha x = 20$  (Raether's limit) [21]. Above this value, a continuous discharge regime can be generated with spark production.

### **Pulse formation**

As the electrons and ions drift towards the anode and cathode respectively, a pulse signal is induced in the electrodes. These signals are picked up by a readout system.

### **Discharge quenching**

In RPCs, the discharge is quenched by the following mechanisms:

1. prompt switching off of the field around the discharge point, due to the large resistivity of the electrodes: the duration of the discharge is much shorter than the relaxation time of the electrode plates [22], which is of the order of  $\rho\varepsilon = \tau \approx 2$  s for glass ( $\rho$  and  $\varepsilon$  are the resistivity and electrical permittivity). Therefore, the charge needed for furnishing a spark cannot flow fast enough.
2. UV photon absorption by the gas, preventing secondary discharges from gas photoionization.
3. Capture of the outer electrons of the discharge due to the electron affinity of the gas mixture, which reduces the size of the discharge and possibly its transversal dimensions.

### **Rate capability**

The high resistance of the electrodes, which avoids sparks and other dangerous processes (like permanent discharges) represents on the other hand one of the main limitations of this detectors. After the signal is produced, the charge of the avalanche stays on top of the electrode and during this time the effective field in the region where the avalanche develops will be lower. As a consequence, if the counting rate is very high, one can expect fluctuations in the local field caused by earlier avalanches. The main consequence is a reduction of the efficiency and the time resolution.

## Modes of operation

RPCs may be operated either in *avalanche* mode or in *streamer* mode:

- The *avalanche mode* corresponds to the generation of a Townsend avalanche in the gas gap, following the release of primary charges by the incoming radiation. Because of the low amplification of the gas mixtures used in this mode, the gain has to be compensated by using high-gain fast amplifiers integrated in the front-end-electronics (FEE)[23].
- The *streamer mode* requires higher operation voltages than the avalanche mode. In this case, the secondary ionizations, caused by photons emitted by excited gas molecules, are so large that the space charge created distorts the electric field, causing eventually a discharge in the detector gas. Quenching gases are added to control and localize this discharge. On the one hand, this approach has the advantage of providing larger signals that can be discriminated without amplification. However, due to high resistivity of the electrodes, the area where the streamer develops is blind during a given transit time [24].

Originally, RPCs have been operated in the streamer mode. Later on, remarkable progress was achieved in the avalanche mode operation, providing better rate capability of the RPCs. At present, most of the RPCs used for timing operate in avalanche mode.

## RPC designs

**Single gap RPC.** The original RPC [18], had a single gas gap delimited by bakelite resistive electrodes. These counters have evolved since then. Glass electrodes, having a mechanical rigidity and surface quality much superior to bakelite, are being used in recent designs.

**Multigap RPC.** This construction method has been proposed in 1996 [25]. It consists on a stack of equally-spaced resistive plates that divide the gas volume into a number of individual gaps. High voltage is applied to external surfaces. Initially, internal plates take correct voltage, from electrostatics, then they are kept at correct voltage by flow of electrons and positive ions created by the avalanches in the gaps. This feedback principle produces a similar gain in all gas gaps. Due to the fact that resistive plates are transparent to fast signals, the readout is done at the most external plates [24]. This design presents an improvement in the efficiency and time resolution. A possible drawback of this design are the high voltages required.

Multigap RPCs have been used to construct large area time-of-flight detectors [26] delivering a time resolution of the order of  $\sigma(ToF) < 60$  ps for minimum ionizing particles (MIPS). Some examples are the ToF detectors for the ALICE [27], STAR [28], HADES [29] or FOPI [2] experiments.

ALICE and STAR use a very similar approach for their timing RPCs. Both designs consist on multigap glass RPCs, where the pickup pads are deposited in a Printed Circuit Board (PCB).

In the ALICE detector, an element consists on a long RPC strip ( $120 \times 7.4$  cm<sup>2</sup>) with 96 readout pads arranged in two rows. The strip is made of 2 stacks of 5 gaps of 250  $\mu\text{m}$  each. The resistive plates are commercial glass 400  $\mu\text{m}$  thick for the internal and 550  $\mu\text{m}$  for the external plates; the distance between them is kept fixed with spacers made of nylon fishing line. The anode is in the middle and the two cathodes are on the external surfaces. For the readout, a differential signal is obtained from the cathode and anode pads.

In the STAR experiment, an RPC element is made of six pads. The size of each pad is  $3.1 \times 6.0$  cm<sup>2</sup>. The glass plates are 520  $\mu\text{m}$  thick. There are six gaps of about 220  $\mu\text{m}$ . The electrodes are made of graphite and the readout is done in the pads.

In the FOPI experiment, an RPC module consists on a 16 strip anode with an active width of 4.6 cm and a length of 90 cm. The gap size is 300  $\mu\text{m}$  with glass plates of 1.1 mm thickness. The shape of the strips has been adapted to the readout cables in order to match the impedance to 50  $\Omega$ .

HADES design is slightly different. It consists on glass and aluminium RPC cells of 4 gaps of 300  $\mu\text{m}$  width. This hybrid design is more appropriate for this experiment, due to the higher rates which can be tolerated by these type of detectors. The cells are electrically isolated in order to prevent the crosstalk.

### 2.1.2 Performances of RPCs

Performances of resistive plate chambers, namely time resolution and efficiency, are determined by different factors such as the gas mixture, the number of gaps, the gap width and the operation voltage. The readout electronics plays also an important role in the time resolution.

#### Gas mixture

Modern standard RPCs working in avalanche mode use mostly mixtures of tetrafluoroethane ( $\text{C}_2\text{H}_2\text{F}_4$ ) with 2% to 5% of isobutane (iso- $\text{C}_4\text{H}_{10}$ ) and 0.4% to 10% of sulphur hexafluoride ( $\text{SF}_6$ ). The addition of  $\text{SF}_6$  has been shown to extend the streamer free operation region [30]. By increasing the

fraction of  $\text{SF}_6$ , the efficiency plateau shifts to higher voltages. The time resolution is defined by to competing processes with increasing  $\text{SF}_6$  concentration. Large fractions of this gas require higher electric fields. As a consequence, a higher drift velocity is expected, which results in an improved time resolution. On the other hand,  $\text{SF}_6$  can capture all electrons in a cluster of ionization due to the large capture cross-section for low energy electrons, . Thus, by increasing the concentration of  $\text{SF}_6$ , the number of ionization clusters that generate an avalanche is reduced, leading to a degradation of the time resolution and efficiency (Fig. 2.1).

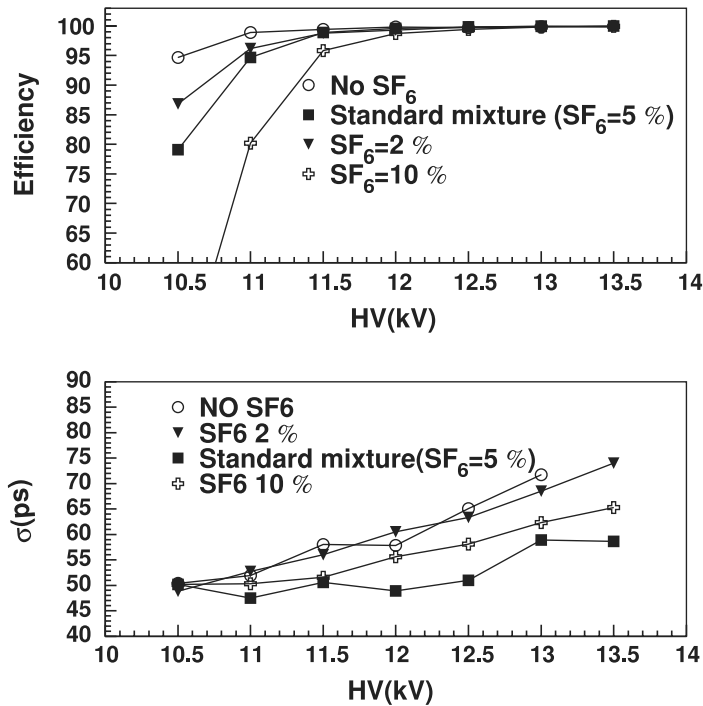


Figure 2.1: Efficiency (top) and time resolution (bottom) for different  $\text{SF}_6$  fractions used in the gas mixture [30].

### Size and number of gaps

The size of the gap is a factor that determines, in a significant way, the efficiency and the time resolution that can be achieved with an RPC detector. The larger the gap, the higher the efficiency. Gaps of around 2

mm were used in the first designs [18] and are used nowadays in the so-called *trigger RPCs*, operated either in *avalanche* or *streamer* mode. This type of detectors have reached efficiencies above 98% per gap, independently of the operation mode. The time resolution achieved is between 1 and 1.5 ns ( $\sigma$ ).

Thinner gaps show a reduced efficiency ( $\varepsilon = 75\%$ ), but the time resolution increases in a significative way. Resolutions better than 90 ps ( $\sigma$ ) have been obtained using gaps ranging from 200 to 300  $\mu\text{m}$ . On the other hand, it was observed that for gaps smaller than 200  $\mu\text{m}$ , apart from the mechanical difficulties, such as the uniformity of the gap, the time resolution deteriorates. By using multigap RPCs one can improve the efficiency in small gap chambers. In fact, the efficiency increases with the number of gaps as [24]:

$$\varepsilon = 1 - (1 - \varepsilon_g)^n \quad (2.2)$$

where  $\varepsilon$  is the total efficiency,  $\varepsilon_g$  is the efficiency of one gap, and  $n$  is the number of gaps. The time resolution also improves but with  $\sqrt{n}$ .

### Operation voltage

Another important factor which determines the performances of an RPC is the electric field. Timing RPCs work at fields of 100 kV/cm. The higher this value, the larger the drift velocity and therefore the better the time resolution achieved. The efficiency is also higher with high voltages. It has also to be taken into account that the probability for streamers increases with the voltage. The working point will be a compromise between these factors: high efficiency, good time resolution and low probability of streamers.

### Time-charge correlations

In order to achieve the best possible time resolution available with an RPC, a measurement of the charge induced by the electrons is needed. This charge value is correlated with the time, due to the physics of the RPC [28]. The procedure for subtracting this dependence is often called 'slewing correction'. See figure 2.2 for a sample of this correlation.

Figure 2.3, shows the efficiency, time resolution and streamer probability as a function of the high voltage applied to electrodes for five gaps RPC [27]. As we can see the efficiency reaches 99.9%, and the time resolution is in the 40 ps ( $\sigma$ ) range. Streamers appear for voltages higher than 13 kV in this design.

In table 2.1 a survey of the published results concerning the performances of RPC detectors is shown. All these results concern multigap RPCs with a gas gap ranging from 220 to 300  $\mu\text{m}$ . All the efficiencies reached are

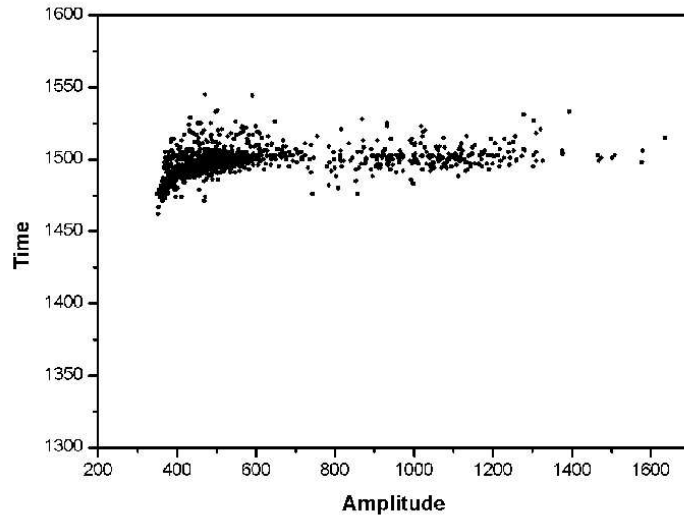


Figure 2.2: The time amplitude correlation for cosmic rays with a multigap RPC (300  $\mu\text{m}$ , gap width) at 14 kV voltage operation. Standard mixture has been used[28].

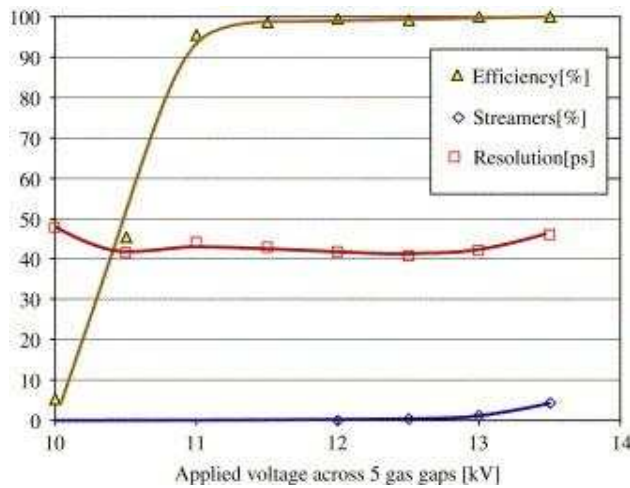


Figure 2.3: Efficiency, time resolution ( $\sigma$ ) and streamer probability for a Multigap RPC [27].

higher than 90%. Results concerning time resolution vary from the 48 ps ( $\sigma$ ) obtained for the ALICE RPCs [27] to the 90 ps obtained by STAR experiment [28]. It should be noted that all these results have been measured using MIPS,

Voltage (kV)	Gap width ( $\mu\text{m}$ )	Number of gaps	$\varepsilon$ (%) $\sigma$ (ps)	Time Resolution	Ref.
14	220	6	90	90	[28]
9.5	300	6	97	<73	[2]
12	250	10	99.9	48	[27]
6.2	300	4	97	67	[29]

*Table 2.1: Reported performances of recent RPC counters. The gas mixture used in all cases is the standard one.*

except for [29], where the fragmentation products of  $^{12}\text{C}$  at 1 GeV/u were used.

### Read-out electronics

Read-out electronics is also an important element in the time resolution which can be achieved with RPC detectors. This is due to the fact that the intrinsic time resolution of RPCs is very good ( $\sigma_i \approx 25$  ps)[31], therefore the total time resolution will be a quadratic sum of the intrinsic and the electronics resolution. Different electronics have been developed in order to minimize this contribution to the total time resolution.

STAR and ALICE experiments used a front-end-electronics (FEE) based in the MAXIM3760 amplifier [32, 28]. Due to the power used by this device (300 mW), people working at ALICE designed a new ultra fast and low power (40 mW/channel) FEE, rejecting MAXIM design. Readout is performed with a high performance TDC developed at CERN [31] whose time resolution is about 20 ps.

For the FOPI experiment, a complete FEE and digitization card has been developed (TAQUILA)[2]. The time resolution of this new electronics is better than 30 ps.

### RPCs and heavy ions

Very little is known about the performance of RPCs for highly ionizing particles such as heavy ions. It has been reported that in fragmentation experiments of  $^{12}\text{C}$  [29] the capabilities of such detectors is not significantly degraded. A resolution of 67 ps ( $\sigma$ ) and efficiency of 97% have been reached for a 4-gap glass aluminium RPC.

For heavier ions, ionization is expected to increase as  $Z^2$ ,  $Z$  is the atomic number of the ion, two effects have to be studied:

- energy losses in the electrodes should not be enough to stop the ion.
- the highly primary ionization would imply necessary a lower field, and subsequently in a reduced value of Townsend first coefficient and drift velocity, so the final resolution achievable will be a competition between these two effects. Efficiency can always be improved just by using additional gaps.

## 2.2 Scintillation detectors

Scintillation detectors are one of the most widely used particle detection devices in nuclear and particle physics. They are based on the fact that certain materials when struck by an ionizing radiation, emit a small flash of light, i.e. a scintillation.

### 2.2.1 General features

The basic elements of a scintillation detector are sketched in figure 2.4. It consists on a scintillating material which is optically coupled to a photomultiplier, either directly or via a light guide. This element matches the scintillator shape to the Photomultiplier's round face and transports photons. The light produced is transmitted to the photomultiplier tube (PMT) where it is converted into a weak current of *photoelectrons*. This current is then amplified by an electron multiplier system. This device consists on a series of dynodes, where when photoelectrons strike the dynode, they cause the emission of secondary electrons, which are accelerated to the next dynode where more electrons are released and further accelerated. An electron cascade down the dynode string is thus created. At the anode, this cascade is collected to give a signal which can be analyzed.

In general, scintillator signals provide a variety of information. Some of the most outstanding properties of this signals are:

**Sensitivity to energy.** Above a certain minimum energy, most scintillators behave in a near linear way with respect to the energy deposited, i.e., the light output of a scintillator is directly proportional to the energy deposited by the particle. Since the PMTs are also linear devices, the amplitude of the final electrical signal will also be proportional to this energy. This is the reason why scintillators can be used as energy spectrometers.

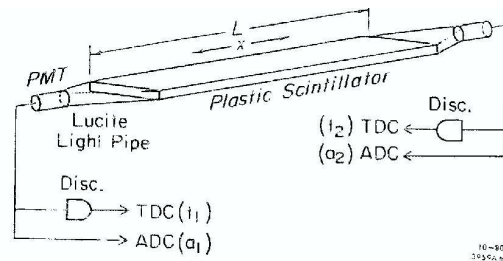


Figure 2.4: Schematic view of a typical scintillation detector.

**Fast time response** Scintillation detectors are fast instruments in the sense that their response and recovery times are short relative to other types of detectors. This fast response makes their use suitable for timing measurements. This feature, together with their fast recovery time also make this detector suitable to accept high counting rates (the decay time of plastic scintillators is  $\tau \sim 1$  ns).

While many scintillating materials exist, not all are suitable as detectors. In general, a good detector scintillator should satisfy the following requirements:

1. high efficiency for conversion of exciting energy to fluorescent radiation
2. transparency to its fluorescent radiation and consequently good transmission of the light
3. emission in a spectral range consistent with the spectral response of existing PMTs.

Nowadays two kinds of scintillator materials are in use: inorganic crystals and organic scintillators. The first ones are slower, but they have excellent properties for  $\gamma$ -detection. Organic scintillators are discussed in the next subsection.

### 2.2.2 Organic scintillator materials

Organic scintillators are aromatic hydrocarbon compounds containing linked or condensed benzene-ring structures. Their most interesting feature is a very rapid decay time, on the order of few nanoseconds or less [21, 20]. This is the reason why these materials are suitable for time measurements.

Scintillation light in these compounds arises from the transitions made by free valence electrons of the molecules. Ionization energy from penetrating

Scintillator (BICRON)	PMT (HAMAMATSU)	$\sigma$ (ps)	Ref
BC422Q(0.5%)	R4998	8.9	[33]
”	R2083	11.2	[33]
”	R3809U	24.8	[33]
”	R5900-L16	19.8	[33]
BC404	R6504S	49	[35]
BC408	R2490-05	50	[34]
BC420	R2431	75	[9]

Table 2.2: Time resolution achieved with scintillators in different experiments

radiation excites both the electron and vibrational levels. Because of the energy lost by vibrational quanta, emission and absorption spectra are shifted in wavelength, thus scintillator is transparent to the light it produces.

Due to the molecular nature of luminescence in these materials, organic scintillators can be used in many physical forms without the loss of their scintillating properties. As detectors, they have been used in the form of pure crystals and as mixtures of one or more compounds in liquid and solid solutions.

### 2.2.3 Performances of scintillation detectors

Organic scintillators have been the most used detectors in ToF measurements. Recently the development of new fast plastic scintillators and ultra-fast photomultiplier tubes, has allowed reaching very good time resolutions [33, 34, 35].

A survey of the latest results obtained for the time resolution with scintillation detectors is presented in table 2.2.

As we can see, the best results correspond to reference [33], where the time resolution achieved for  $^{40}\text{Ar}$  at 95 MeV/u is better lower than 20 ps ( $\sigma$ ), reaching 9 ps for a specific scintillator (BC422Q) and PMT HAMAMATSU R4998. It should be taken into account that these measurements have been performed using small detectors (about 50 mm long). In a realistic environment, the size of the scintillator should be large enough to cover a large acceptance. Also, it would be important to keep the distance between the

beam line and the PMTs to avoid extra radiation damage of the tubes. Not so good time resolution is expected for a larger scintillators due to the reduction of the number of photons transmitted to the PMT. The thickness of the scintillators was 0.5 mm. In principle, the use of thinner material in the beam line is required in order to avoid extra interactions and energy straggling of the incident beam. In contrast, with this requirement, time resolution decreases due to the reduction of the photon emission. In fact, the time resolution is related to the number of photoelectrons ( $N_{p.e.}$ ) by the following empirical relation [33]:

$$\sigma_T \propto (N_{p.e.})^\alpha \quad (\alpha = -0.5) \quad (2.3)$$

The type of the PMT plays an important role in the time resolution obtained with scintillation detectors (see table 2.2). Comparing the excellent time resolution obtained with the R4998 and the R2083 PMTs, a resolution much worse is obtained with the R3809U and R5900-L16 despite of the faster timing response (0.15 and 0.6 ns risetime versus 0.7 ns). This might be due to the very fast time response of the R3809U photomultiplier relative to the time duration of the scintillating light. This fact suggests the importance of selecting the scintillation materials and the PMTs considering the matching of their properties.

The time resolution due to electronics (discriminator and TDC) contributes to the total time resolution. In Ref. [33], this contribution has also been estimated and its value is better than 8 ps ( $\sigma$ ), very close to the TDC precision (7.2 ps  $\sigma$ ). Therefore the precision of the electronics becomes not negligible for a high resolution ToF scintillation detector below 10 ps.

The result of reference [34] correspond to a more realistic setup. The beam used was 2 GeV  $\pi^-$ . The scintillators were 165 and 130 cm long with a double layer configuration. The thickness of each plastic was 5 cm allowing a better statistics of photoelectrons. The use of a double layer system allows a better time resolution than a single one (65 and 50 ps  $\sigma$  respectively).

In [35], the resolution achieved with a  $95 \times 10 \times 2$  cm<sup>2</sup> if 49 ps for negative pions. The readout electronics consisted on an ADC (LeCroy 2249 W, 0.25 pC/count) a TDC (Phillips 7186, 25 ps/count) and a discriminator (Phillips 708).

It should be taken into account that these resolutions have been obtained by using the time-walk correction of signals. This correction is due to the pulse height variations. The times measured are corrected by the integrated charge of the PMT by:

$$T = T^{raw} - \frac{C^{walk}}{\sqrt{q}} \quad (2.4)$$

where  $T$  is the corrected time,  $T^{raw}$  the uncorrected time,  $C^{walk}$  the correction factor and  $q$  the integrated charge of pulse. Results of [9], correspond to the resolution achieved for fission fragments. The size of the scintillator used was 1m long.

## 2.3 Summary and conclusions

Resistive Plate Chambers and scintillator detectors are very suitable devices for the measurement of the time-of-flight of residues produced in nuclear reactions induced by relativistic heavy ions. The efficiency and time resolution achieved with the ‘state of the art’ timing RPCs, multigap glass RPCs in a range of 0.2-0.3 mm gap width, is about 99% and 50 ps ( $\sigma$ ) respectively for MIPS. These results are very encouraging for the use of these type of detectors in the identification of heavy ions by time-of-flight measurements, as an alternative to the standard scintillation detectors. Scintillators have shown excellent performances for new scintillation materials and photomultiplier technologies.

Recent experiments [2, 27, 28, 29] have implemented large area ToF walls based on RPC technology due to very good performances and the lower cost per channel compared with the scintillator option.

However, further studies should be performed in order to investigate the performances of RPCs with heavy ions.



# Chapter 3

## Performance tests of different read-out electronics

In this chapter are presented the results obtained in the evaluation of different solutions proposed for the readout of the signals induced by heavy ions in plastic scintillators and RPC detectors, in order to achieve the time resolution required for the ToF wall (Sect. 1.3).

The first option is the use of standard modular electronics (Discriminators, TAC and ADC). Another possibility is a complete digitation of the signals produced by fast scintillators and PMTs and an offline analysis of them with software tools. The last possible solution is the use of integrated electronics, in particular the TAQUILA card developed by the Electronics department at GSI [2].

### 3.1 Standard modular electronics

The first option we have evaluated is the use of standard modular electronics (NIM and VME) for the readout of the signals.

#### 3.1.1 Experimental Setup

In order to measure the time resolution that can be achieved with this method, we used the setup shown in figure 3.1. The signals produced in both PMTs were sent to ORTEC constant fraction discriminators (CFD) [36]. One of the signals was delayed before being sent to the Time to Amplitude Converter (TAC) as STOP signal. The other pulse was used as START. The TAC output is sent to an Analog to Digital Converter (CAEN V785 ADC) for on-line analysis of the distributions of TAC amplitudes, given by the

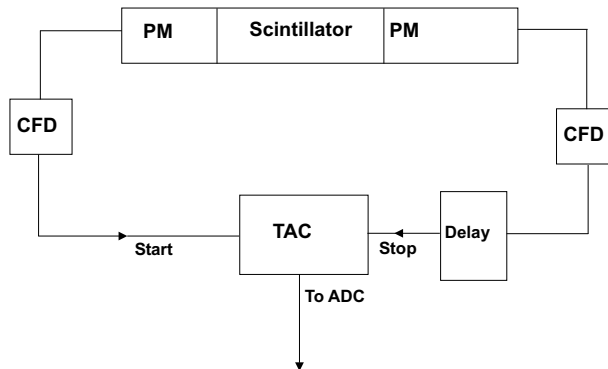


Figure 3.1: Experimental setup used for the test with modular electronics.

left-right time differences.

In order to calibrate TAC+ADC system we just changed the delay on one of the signals, measuring the corresponding ADC channel. The obtained data were fitted to a straight line, being the slope of this fit is the calibration factor. In this case, the slope value we obtained was 5.42 ps/ch.

Once the TAC and ADC have been calibrated, we can analyze the different contributions to time resolution, electronics and scintillator and PMT.

### 3.1.2 Results

#### Electronics

In order to measure the contribution of electronics to time resolution, we have used a Lecroy Pocket pulser ( $\sim 1.5$  ns rise time ) to simulate the PMT signals. The time resolution is given by the width of the gaussian fit of the ADC spectra. Different configurations of the setup were investigated in order to optimize the time resolution, e. g., changing thresholds and shaping delays of CFDs. The best result obtained was ( $\sigma_{elec} \approx 8$  ps).

#### Scintillator and PMTs

In order to produce the scintillation in the plastic (BICRON BC420), we used a U.V laser impinging at the center of the scintillator. Different values of the voltage in the PMTs (HAMAMATSU R2431) and in the intensity of the laser were tested to analyse the contribution of these two factors to the time resolution. The resolution is again given by the width of the gaussian fit of ADC spectra (Fig. 3.2).

In table 3.1, the time resolution for different values of the voltages of the photomultipliers and different intensities of the laser are shown. The intensity

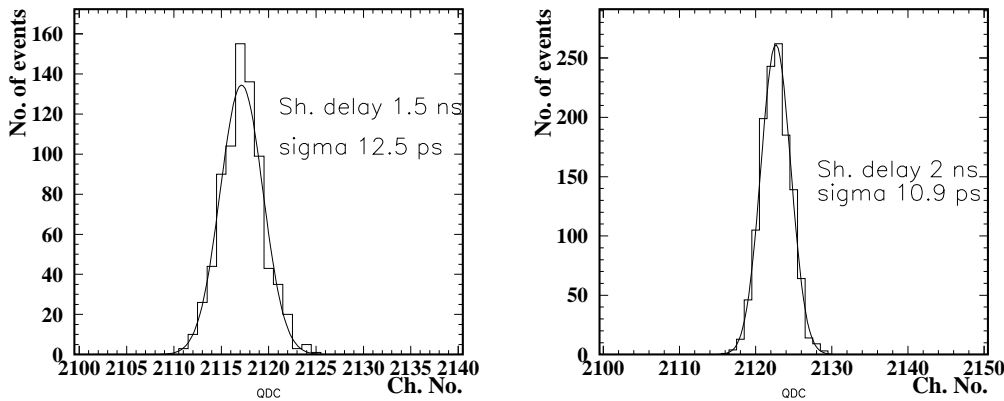


Figure 3.2: ADC spectra for the scintillator and PMTs. Sigma is the width of the distribution times the calibration factor.

of the laser is determined by the amplitude of the output signal. As we can see, the higher the light intensity, the better the time resolution achieved. This observation is in agreement with eq.(2.3), since a higher light intensity produces a larger number of photoelectrons. One can also see that the time resolution does not improve by increasing the voltage. This fact might be due to the appearance of noise in the phototube. Therefore the time resolution estimated for the scintillator and PMT system is around  $\sigma \approx 8$  ps.

## 3.2 Signal digitation and pulse shape analysis

As mentioned before, this method is based on the complete digitation of the pulses produced by the detector and the analysis of these pulses by means of software applications. This procedure has been used in recent experiments [37] and represents the state-of-the-art in data analysis and discrimination techniques.

In this section we present the results obtained in the analysis of the pulses produced by plastic scintillators coupled to fast photomultiplier tubes. We also analyzed the signals produced by a Lecroy pocket pulser in order to distinguish between the two different contributions to the time resolution. On the one hand, the time spread due to the propagation of the light within the scintillator and the photomultiplier features (rise time and transition time spread). On the other hand, the contribution due to the readout itself (digitation sampling rate and analysis method.)

High Voltage (V)		Sh. Delay (ns)	Output (V)	$\sigma_{intrinsic}$ (ps)
Left	Right			
1500	1200	2	-5.0	16.3
1200	975	1	-5.0	23.9
1200	975	2	-1.5	16.5
1200	975	1.5	-5.0	9.7
1200	975	2	-5.0	7.4
3000	2440	2	-6.0	85.7

Table 3.1: Time resolution of the scintillator and PMT for different configurations of the setup. The output is the amplitude of the pulse produced by each PMT, left and right.

### 3.2.1 Experimental Setup

In order to investigate the time resolution that can be obtained by means of a complete signal digitation method, we have used the setups shown in the figure 3.3.

The first setup used in this experiment (Fig.3.3-left) consisted on a BC420 plastic scintillator (20 cm long, 4 cm high and 5 mm thick) coupled to two Hamamatsu 2431 photomultiplier tubes (PMT) placed at both sides of the scintillator. Neither light guides nor optical grease were used. In order to measure the time resolution, one of the outputs was delayed and both were connected to two of the channels of a digital oscilloscope (Tektronix TDS-7404) [38], thus we had two values for the time and the possibility to measure left-right time difference.

The plastic was excited with a UV laser always impinging at the center

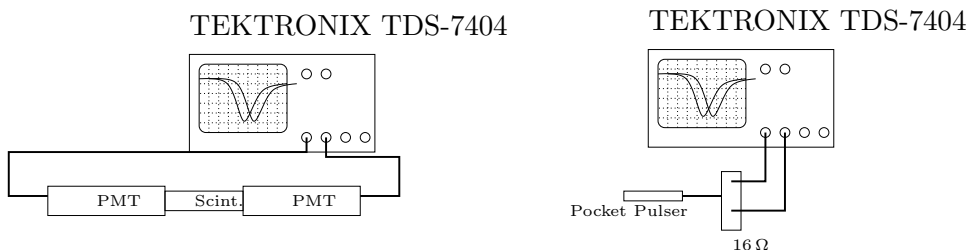


Figure 3.3: Experimental setups used for the acquisition of signals and pulse shape analysis.

of the scintillator. Trigger was one of the channels of the oscilloscope.

The second setup (Fig. 3.3-right) was almost identical, but the input signals were produced by a pocket pulser whose output was splitted.

The oscilloscope used in this test digitizes at 10 GS/s, so we had a bin size of 100 ps in time axis. The resolution in the y axis, which corresponds to the amplitude of the signal, was 8 bits, therefore the signals were recorded in 255 different values of the amplitude.

The signals recorded during the experiment were saved in binary files and then analyzed with a program developed for this purpose (*PIFFIA*)[39]. Details of this program will be given in next subsection.

Figure 3.4 is an example of the signals provided by both setups. Left panel shows the pulse produced by the scintillator coupled to the PMTs. Rise time and width of the signal are  $\sim 2.5$  and  $\sim 5$  ns, respectively. In the right panel, the signal produced by the pulser is shown. Rise time values of this pulse are shorter than the ones produced by the scintillator (Rise time  $\sim 1.3$  ns and width  $\sim 5$  ns).

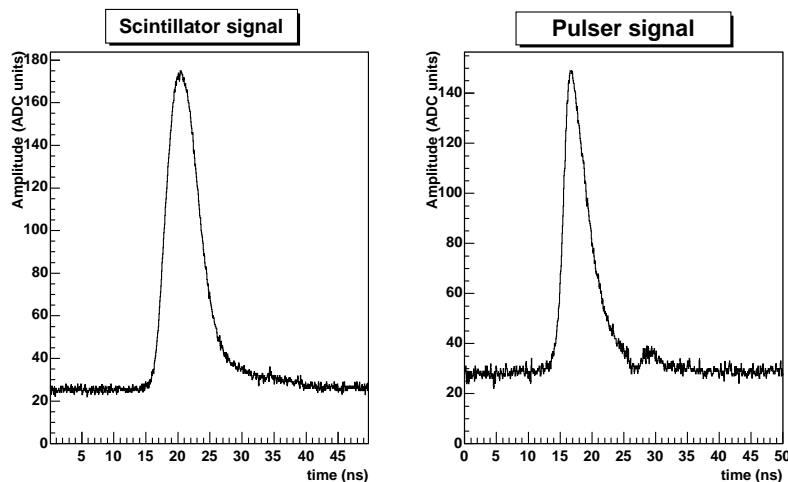


Figure 3.4: Left: output signal of one of the PMTs. Right: output signal of the pocket pulser. We can see that the left pulse is slower than the right one.

### 3.2.2 Analysis software (PIFFIA)

PIFFIA is the acronym of Particle Identification of Fission Fragments by Ionization Analysis. This program is a user interface and front-end for the simulation, graphical analysis and evaluation of fission data. Its first application was the analysis of fission fragments ionization on twin-ionization

chambers. Due to the modularization of the code, PIFFIA allows the use of alternative algorithms. PIFFIA code is written in C++, an Object Oriented programming language, and uses all the power of the ROOT framework for histogramming, curve fitting and graphical visualization [40].

Like most of the software developed in C++, PIFFIA is constituted by a set of classes. There is a manager class, `Piffia`, which controls the event loop for the event readout and analysis. Another important class is `PiffiaConfig`, a configuration class which allows the user to control the values of all the configuration parameters, such as fitting intervals, thresholds, etc.. As far as our analysis is concerned, there are two important classes. The first one defines all the parameters which characterise the signal, (`PiffiaSignalObs`) such as maximum voltage of the signal, etc. The second one calculates the parameters defined in the first class (`PiffiaObsAnal`).

In order to adapt PIFFIA to the analysis of scintillator signals, new classes were added to the original code. They define the new configuration and signal parameters and the new analysis algorithms<sup>1</sup>. The new defined parameters are listed in table 3.2. Except for the `ConstantFractionTime`, all the parameters listed are either values obtained from the signal and its derivative, or parameters calculated by fitting these curves.

Figure 3.5-top-left shows the definition of the signal parameter `timeSignalBegin1`. As we can see, this parameter is the crosspoint between two linear fits: the fit of the baseline and the linear fit of the leading edge of the pulse. In figure 3.5-top-right, the definition of `timeSignalBegin2` parameter is shown. The definition of these two signal parameters is almost the same. The only difference is that the fit of the leading edge is parabolic instead of linear. In figure 3.5-bottom, the derivative of the digitized pulses is represented. The definition of `delayDerivative` parameter is also shown. It is the crosspoint of the derivative baseline and the linear fit of the derivative leading edge.

The Constant-Fraction-Time is obtained by the following method: First of all, the pulse is inverted and attenuated by a factor that can be defined as configuration parameter (`attenuationFactor`). Then the inverted-attenuated signal is summed to the original signal but delayed by a certain number of bins. This value can also be changed (`shapingDelay`). Until this point, it works like a *hardware* constant fraction discriminator does. To obtain this parameter two linear fits are done:

1. Linear fit of the base line.
2. Linear fit of the summed signal between maximum and minimum.

---

<sup>1</sup>`PiffiaToFConfig`, `PiffiaToFSignalObs` and `PiffiaToF0bsAnal`, respectively

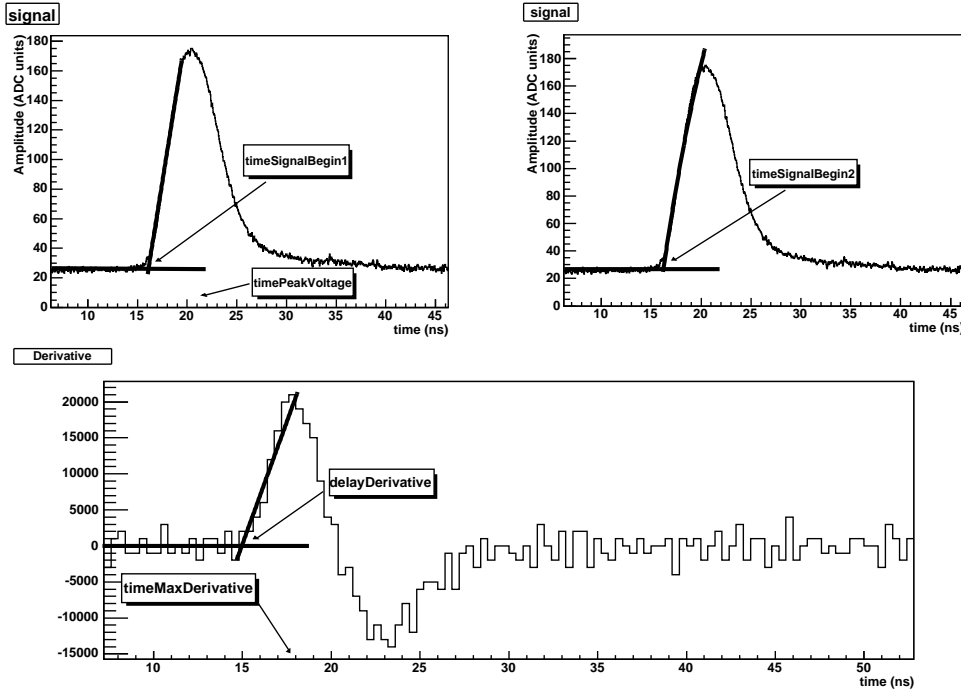


Figure 3.5: Definition of some signal parameters.

The `ConstantFractionTime` will be given by the crossing point of both linear fits (See figure 3.6).

There is another class which stores each pair of left-right signals parameters and has the definition of all the ways of computing time: (`PiffiaToFPairObs`). The time is obtained by the following method:

Once all the parameters listed in table 3.2 have been calculated, they are stored in different branches depending on whether they are *Left* or *Right* events. The ways of computing the time is the following:

- The left-light difference is calculated for each of the time parameters defined (`timePeakVoltage`, `timeSignalBegin1`, `timeSignalBegin2`, etc). Based on the parameter `timeAtXPercent`, a new time parameter is defined. This is the so-called *Double discrimination*. It consists on obtaining the crossing point of the baseline and the line which joins the two points where two fractions of the maximum voltage are reached in the leading edge. For instance *Double Discrimination (20% 60%)* is the crossing point of the baseline and the line that joins the points  $0.2 \times Amplitude$  and  $0.6 \times Amplitude$  in the leading edge of pulse.

Name	Description
Amplitude	Value of the maximum voltage of the signal (in ADC units).
timePeakVoltage	Time of the maximum voltage of the signal.
timeSignalBegin1	Crosspoint of the linear fit of the leading edge of the signal and the base line.
timeSignalBegin2	The same as timeSignalBegin1, but the fit is parabolic.
max(min)Derivative	Maximum (minimum) value of the derivative.
delayDerivative	The same as timeSignalBegin1, but for the derivative.
timeAtXPercent	Time at diferent percentages of the maximum voltage (X= 20, 40, 60, 80).
timeAtFixedThreshold	Time when the signal reaches a determined value.
ConstantFractionTime	Contant Fraction time by software (See text for details).

Table 3.2: Description of the different parameters used for the characterization of the signal. The names correspond with the ones used in the PIFFIA program.

### Operation of PIFFIA

1. Data acquired with the oscilloscope are readout sequentially from binary files.
2. Signals are analyzed in an event-by-event basis to determine the parameters. Several checks on the signal quality are also performed.
3. The value of all parameters characterising a signal are stored in different leaves of a ROOT *Tree* in order to be able to access to each one easily, e.g., with a ROOT *Browser*.

In order to obtain the time resolution asociated with the different parameters used to define the time, their respective values are stored in histograms.

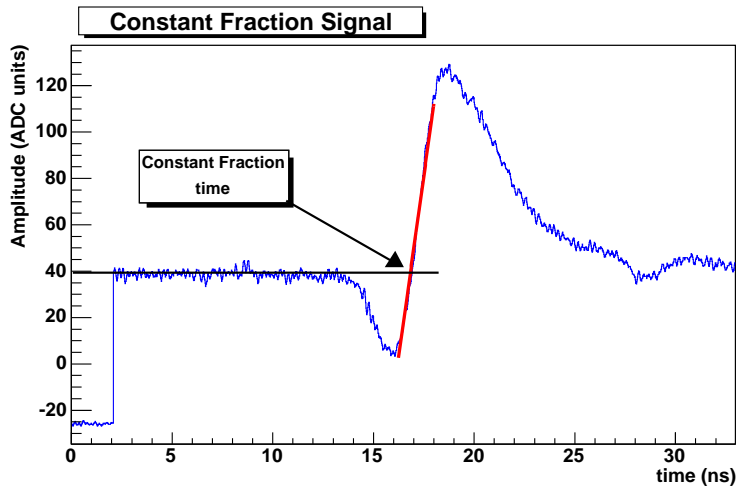


Figure 3.6: Constant fraction signal and details of the calculation of the observable *ConstantFractionTime*. Horizontal Line: Linear fit of base line. The other line is a linear fit of the signal between the maximum and minimum of the signal.

The resolution will be given by the width of the gaussian fit of the distribution of these histograms.

### 3.2.3 Results

The results obtained from the analysis of the signals recorded with the experimental setup described in section 3.2.1 are presented in this subsection.

#### Pocket pulser

The analysis of the signals produced by the pocket pulser makes possible to obtain the contribution to total time resolution due to the readout and pulse shape analysis method.

Figure 3.7 shows the distributions of some of the parameters calculated. These distributions have been obtained from the analysis of 14000 signals produced by the pocket pulser. As we can see, in some of them it is possible to distinguish two peaks corresponding to the left and right channels (bottom-left and right panels). The narrowest distributions are obtained for the parabolic fit of the leading edge of the pulse (bottom-left) and the constant fraction (bottom-right). In figure 3.8, we show the histograms obtained for the left-right time differences.

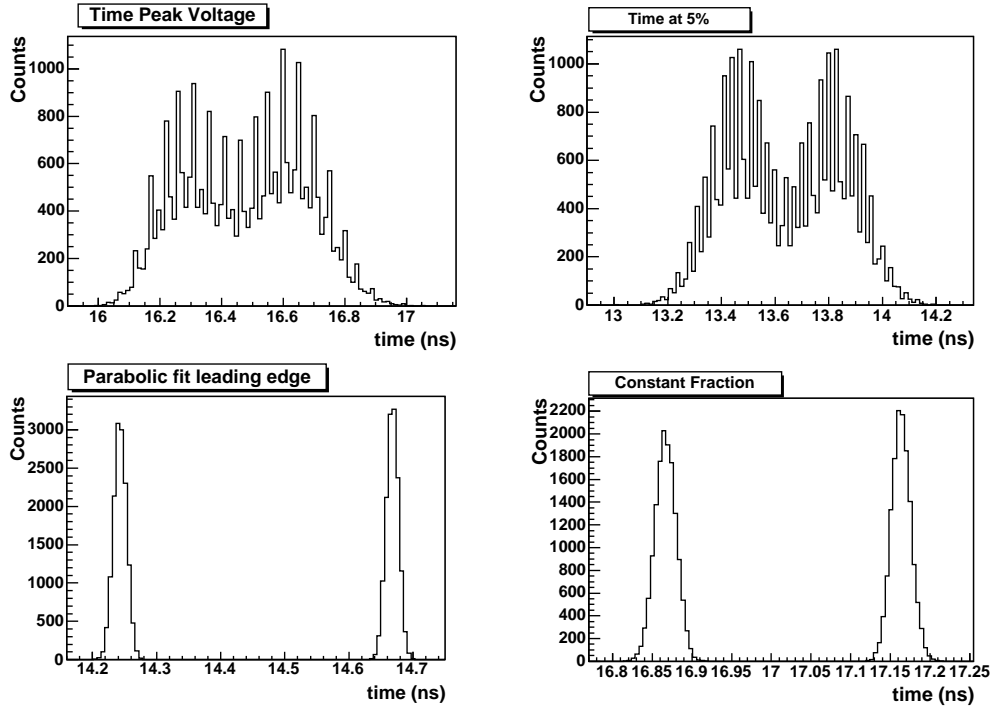


Figure 3.7: Distributions of different pulse parameters for 14000 events with the pocket pulser. Top-left: Distribution of time when the peak voltage is reached. Top-right: Time at 5 per cent of the peak voltage. Bottom-left: Histogram representing the distribution of the observable `timeSignalBegin2` defined in table 3.2. Bottom-right: Distribution of constant fraction time for 0.4 attenuation factor and 208 bins of shaping delay. We can see they have the narrowest peaks.

Table 3.3 presents the time resolution achieved for each of the parameters defined to characterise the signal. As we can see, depending on the parameter, the time resolution achieved ranges from 150 ps ( $\sigma$ ) of the Peak Voltage to the 9.6 ps of the constant fraction. We also see that for a fixed percentage of the signal, there is an optimum range between 40 and 60 percent of the peak, where the resolution is lower than 30 ps. Double discrimination presents its best value in 40%-80% ( $\sigma \approx 30$  ps).

For the derivative of the signal, obtained with the following relation:

$$Der = \frac{A(t + \Delta t) - A(t)}{\Delta t} = \frac{\Delta A}{\Delta t} \quad (3.1)$$

where  $A$  is the amplitude of the signal, the distributions of the observables are wider than the signal itself (Fig. 3.9). This could be due to the number

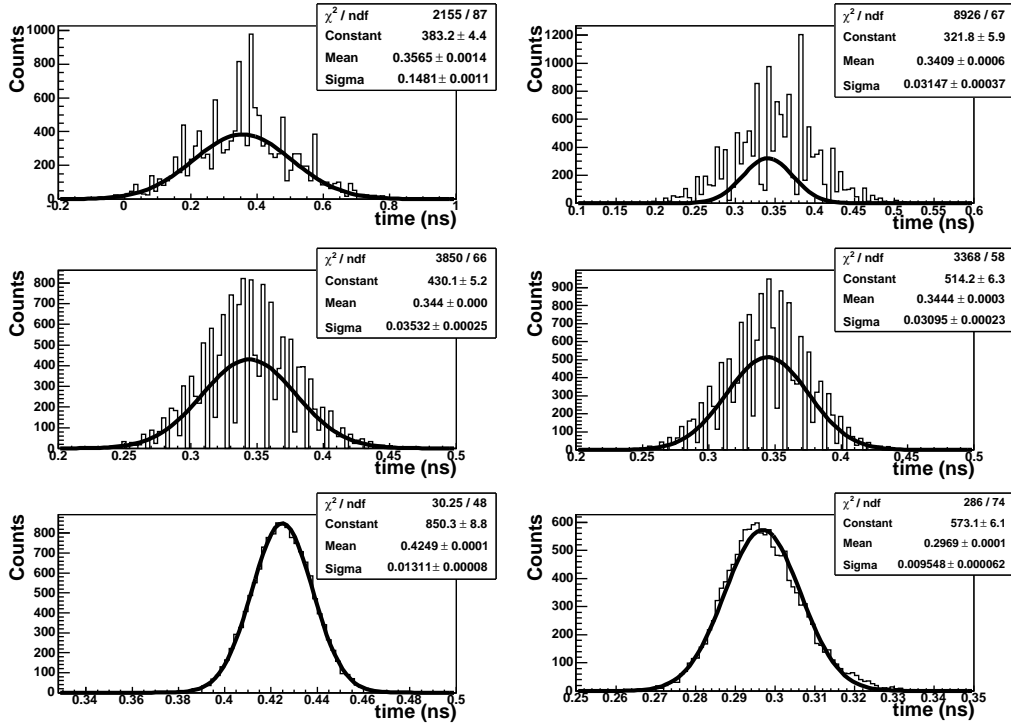


Figure 3.8: Histograms representing the distributions of the time differences for different observables calculated with PIFFIA. Top panels: Left: time at 5% of the peak voltage. Right: time at 20%. Middle panels: Left: Double Discrimination (20%-80%). Right: Double Discrimination (20%-60%). Bottom panels: Left: Parabolic fit of leading edge. Right: Constant Fraction. Resolution is given by the  $\sigma$  of the distributions' gaussian fits. The best result is the one obtained for the constant fraction  $\sigma = 9.6$  ps (bottom-right).

of bins, which is not enough for making a good fit of the leading edge for the derivative. The reason for this is that the precision in A is only one bit, but for the time is  $10^{-2}$ , so the precision for the derivative is

$$\frac{\sigma_{Der}}{Der} = \sqrt{\left(\frac{\sigma_{\Delta A}}{\Delta A}\right)^2 + \left(\frac{\sigma_{\Delta t}}{\Delta t}\right)^2} \quad (3.2)$$

and, if the resolution in the time is much bigger than the resolution of the amplitude, the precision in the derivative is almost the same than amplitude's.

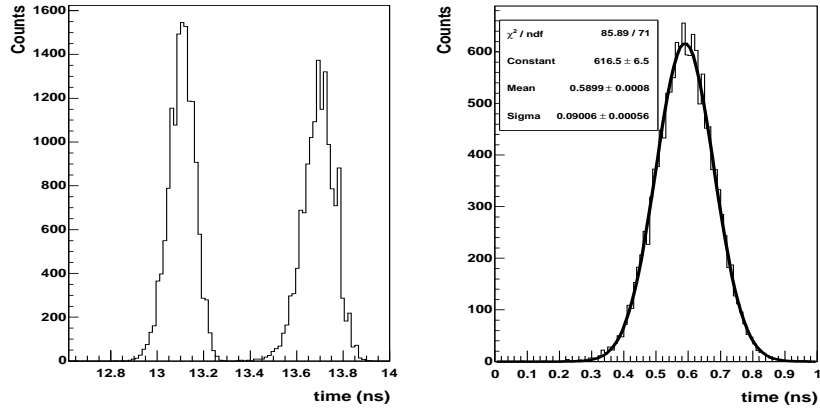


Figure 3.9: Distribution of the parameter *delayDerivative* (see definition in table 3.2) and the corresponding right-left time value. As we can see the resolution is  $\sigma = 90$  ps.

### Scintillators and PMTs

In figure 3.10 we can see the distribution of the time measurements obtained from the analysis of the signals produced by the experimental setup of figure 3.3-left. The widths of the distributions are wider than the ones obtained with the pocket pulser (Fig 3.7). Table 3.3 presents a survey of the time resolutions obtained for each of the parameters. The resolutions achieved are worse than the ones obtained with the pocket pulser. This is due to the fact that scintillator and PMT have intrinsic time resolutions. These factors are due to the decay time of the scintillator, and the efficiency of the PMT. As mentioned in subsection 2.2.3, the time resolution is related with the number of photoelectrons produced. The narrowest distribution corresponds again to the constant fraction in software method ( $\sigma = 16$  ps).

From the results obtained for the time resolution in both experimental setups, we can give an estimation of the scintillator and PMT contribution to the time resolution. Assuming that all contributions are gaussian, the relation between the total resolution and the intrinsic resolution of the plastic scintillator and PMTs is given by

$$\sigma_{TOTAL} = \sqrt{\sigma_{meth}^2 + \sigma_{plastic\&PMT}^2} \quad (3.3)$$

where  $\sigma_{meth} \approx 9.6$  ps is the contribution due to the readout and pulse shape analysis method and  $\sigma_{plastic\&PMT}$  is the resolution of the plastic, the tube and the light propagation within the scintillator.

Parameter	Time Resolution (ps)	
	Pulser	Scintillator
ConstantFractionTime	9.6	16.0
DoubleDiscriminator(20%-60%)	30.9	36.1
DoubleDiscriminator(20%-80%)	35.3	37.5
DoubleDiscriminator(40%-80%)	29.8	38.0
DelayDerivative	90.1	150.0
TimeAtFixedThreshold	50.4	60.2
Timeat20Percent	31.5	36.4
Timeat40Percent	22.8	38.1
Timeat60Percent	27.3	40.5
Timeat80Percent	44.4	52.0
timePeakVoltage	155.0	313.0
timeSignalBegin2	13.1	18.3
timeSignalBegin1	25.9	29.7

Table 3.3: Time resolutions obtained for the parameters used for the characterization of the signal.

From equation (3.3) and the results obtained for the time resolution with the constant fraction method, we can estimate  $\sigma_{plastic\&PMT}$  to be around 12.8 ps. The difference between this value and the one obtained with modular electronics might be due to the resolution in amplitude of the oscilloscope. It should be taken into account that these results have been obtained by impinging the UV laser always at the same point of the scintillator, therefore this resolution is dominated by the statistical nature of the scintillation and the response of the PMTs.

In order to obtain more realistic results of the time resolution which can be achieved by pulse shape analysis some signals obtained with particle beams or cosmic rays should be analyzed using this method.

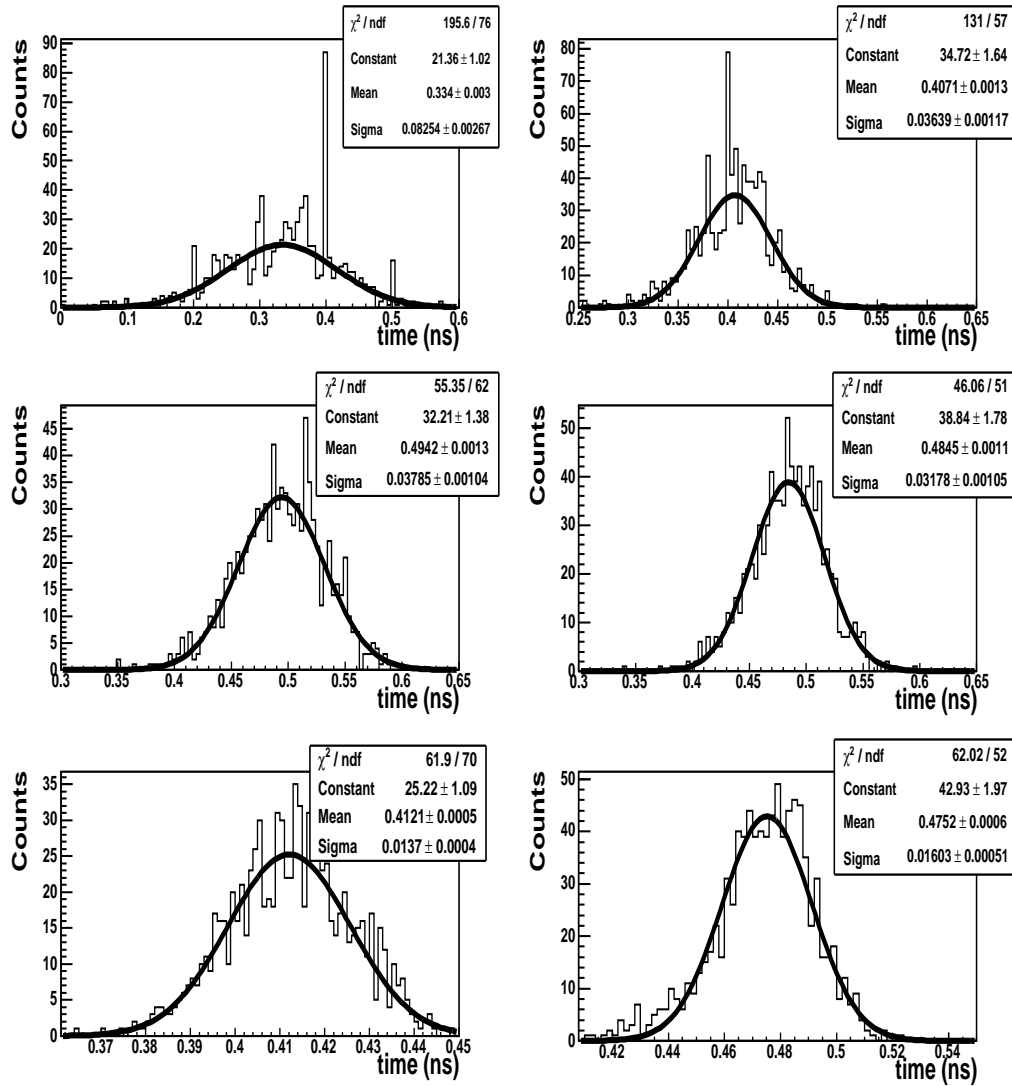


Figure 3.10: Time distributions of parameters shown in Fig. 3.8 for scintillator and PMT signals. As we can see the distributions are wider than the ones obtained with the pulser. The narrowest one is again for the one corresponding to the constant fraction ( $\sigma \approx 16$  ps.)

### 3.3 Integrated electronics:FEE+ TAQUILA digitation card

Another possibility for the data readout is the use of standard electronics. In particular, in this work we have checked the time performances of the Front End Electronics (FEE) and TAQUILA digitation card developed by the electronics department at GSI for the FOPI experiment [2]. It consists on a 16 channel FEE card with a gain of  $\alpha \sim 200$  and a bandwidth of  $\delta f \sim 1000$  MHz. This FEE card has a single ended  $50\Omega$  input and two differential outputs per channel for timing and charge. The amplification is done in three stages. The discrimination of the timing signals is also done in this card.

The FEE card is directly connected to the digitation card (TAQUILA) [2], which contains a 16 channel Time to Amplitude Converter (TAC) system. This TAC is operated in common stop mode: Each signal starts its individual TAC which is then stopped by the next cycle of a 40 MHz master clock (Fig. 3.11). The total charge of the signal is digitized by a QDC. Figure 3.12 shows a picture of the FEE and the TAQUILA digitation card.

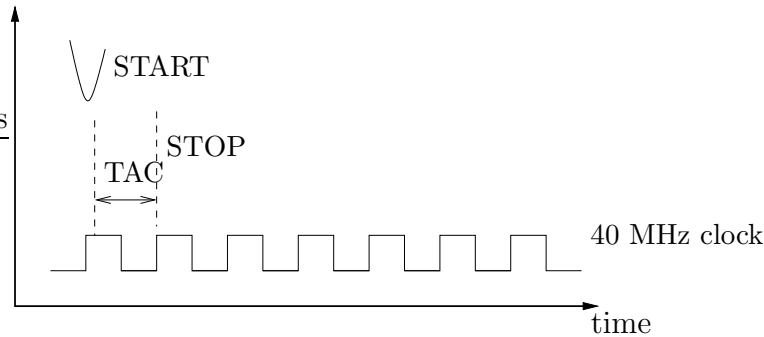


Figure 3.11: Operation of the TAC in common stop mode.

#### 3.3.1 Experimental Setup

In order to determine the time resolution that can be achieved with this new electronics and check whether it is appropriate for our time-of-flight measurements, we have made a test of its performance. The setup used for the test is described in the following.

The input signal was produced by an ORTEC 462 time calibrator [36] (Amplitude  $\sim 230$  mV, risetime 1.5 ns.). This signal was splitted and sent to two different channels of the FEE card. The output signals of the TAQUILA

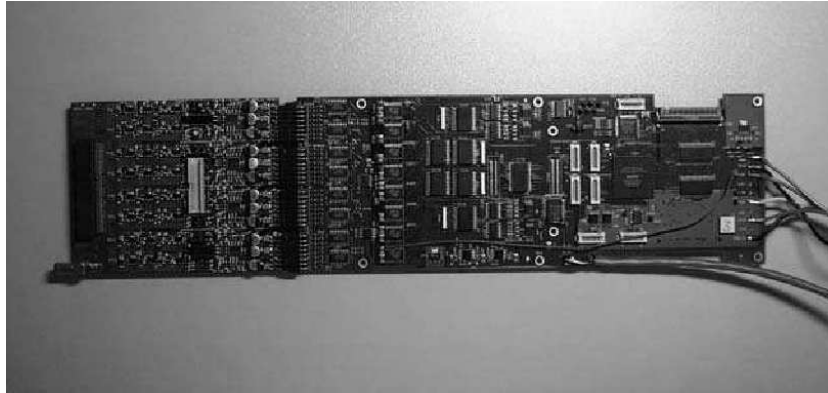


Figure 3.12: The FEE and TAQUILA card

were sent via a GTB bus to a SAM3 VME module [41]. This module was used as readout processor. The acquisition was controlled by the GSI MBS acquisition system. Figure 3.13 shows a diagram of the setup for one of the channels. The information on the charge and time for both channels was saved in a binary file.

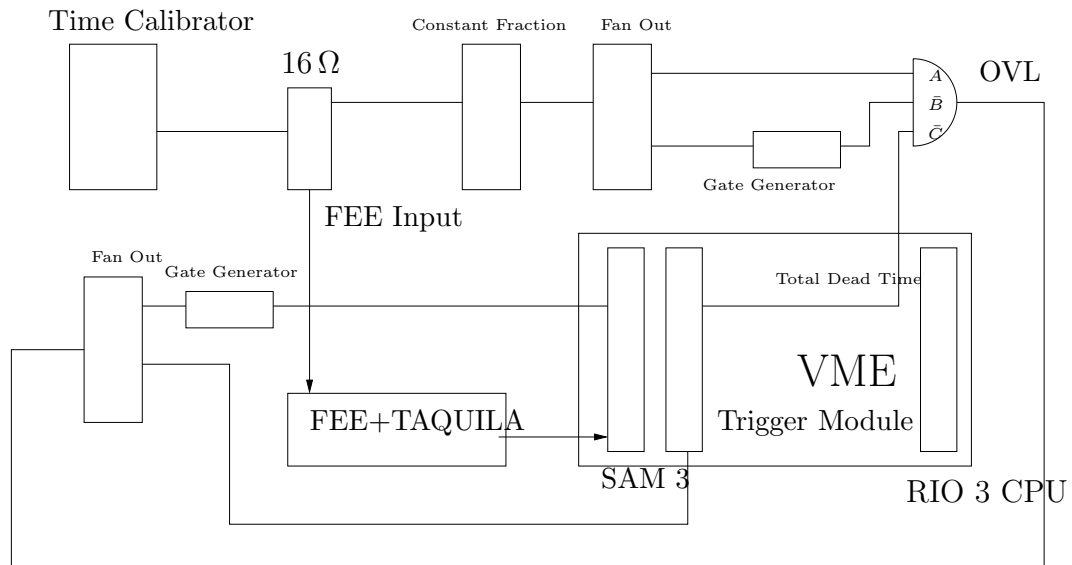


Figure 3.13: Block diagram of the setup and the acquisition system. The upper part corresponds to the gate generators for the acquisition.

### 3.3.2 Results

Figure 3.14 shows the distributions of TAC values for the two channels evaluated in this test. The distributions are almost uniform, except for the first values where we can observe a peak in both channels. This might be due to instabilities of the electronics for very short time differences, and affects only to a small time interval ( $\sim 200$  ps). Even making a cut fo events with time value lower than 300 ps, the number of events lost is less than a 0.5% of the total events. There is a small delay between both distributions. This fact is due to the different lengths of the cables from the signal splitter. The value of the delay can be directly measured in the histograms, and is around 2 channels.

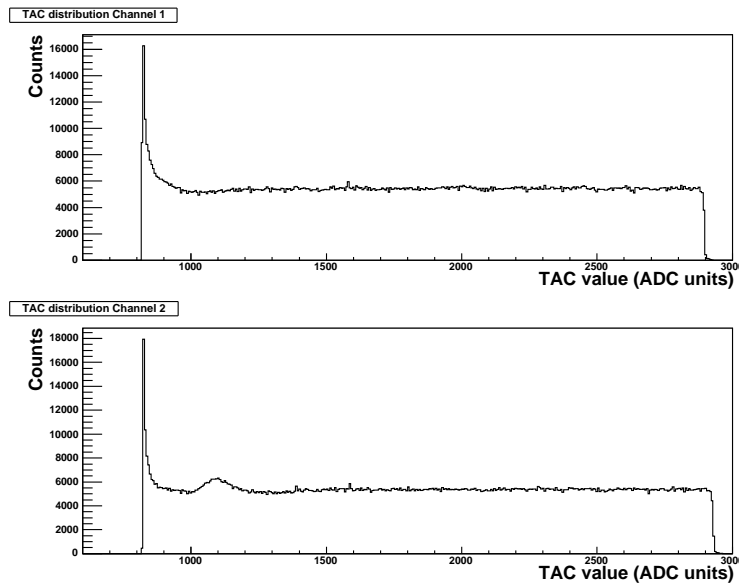


Figure 3.14: Distribution of TAC values for both channels.

For the calibration of the TAC values, we used the fact that the stop is controlled by the 40 MHz clock, therefore, the maximum TAC value corresponds to 25 ns. By counting the number of ADC channels, we can estimate the calibration factors for each channel (Tab. 3.4).

In order to obtain the intrinsic resolution of this electronics, we calculate the difference between time values (TAC value  $\times$  calibration factor) obtained for each channel ( $\Delta T = T_1 - T_2$ ). This values have been obtained by using the calibration factors of table 3.4.

Figure 3.15-top shows the stability of the time difference versus the clocking cycle. As we can see, except for the first values, this value is almost con-

Channel nr.	Nr. of bins	Cal. factor (ps/bin)
1	2147	11.64
2	2176	11.48

Table 3.4: Calibration factors for both channels.

stant. Figure 3.15-bottom-left shows the projection of the time difference, in the interval 5-10 ns, before the correction. As we can see the value of the time resolution, given by the width of the gaussian fit of this distribution is  $\sigma = 25.2$  ps.

As shown in figure 3.15-top-right, the time difference between the channels presents a slightly non-linear behaviour. This behaviour may be corrected by means of a polynomial fit. In order to correct this non linearity, these data have been fitted to a 6th degree polynomial function. By subtracting the fitted values to the original ones is possible to 'straighten up' the distribution and improve the time resolution achieved. Figure 3.15-bottom-right presents the distribution of the corrected time difference, and the time resolution is  $\sigma = 19.8$  ps, therefore, this correction method improves the resolution by a 20%. Other intervals have been checked obtaining similar results ( $\sigma \approx 20$  ps).

### 3.4 Conclusions

In this chapter, we have presented the results obtained from the test of three different readout methods: standard modular electronics, pulse shape analysis and the new TAQUILA electronics.

The time resolution obtained with modular electronics is very good. Intrinsic electronics resolution is  $\sigma_{elec} \approx 8$  ps. and the intrinsic resolution of plastic scintillator combined with the PMTs depends on two factors (see table 3.1), the high voltage applied and the intensity of the laser. Very high voltages produce worse time resolution. This fact could be due to the appearance of noise in the photomultiplier. The second factor is related with the fact that time resolution in scintillation detector is related with the number of photoelectrons, as shown in section 2.2.3. The intrinsic time resolution measured is around  $\sigma \sim 8$  ps.

Results obtained with pulse shape analysis have shown that the time resolution depends on the choice of the signal parameter which defines the time value, ranging from 300 to 16 ps. The best result obtained in this case

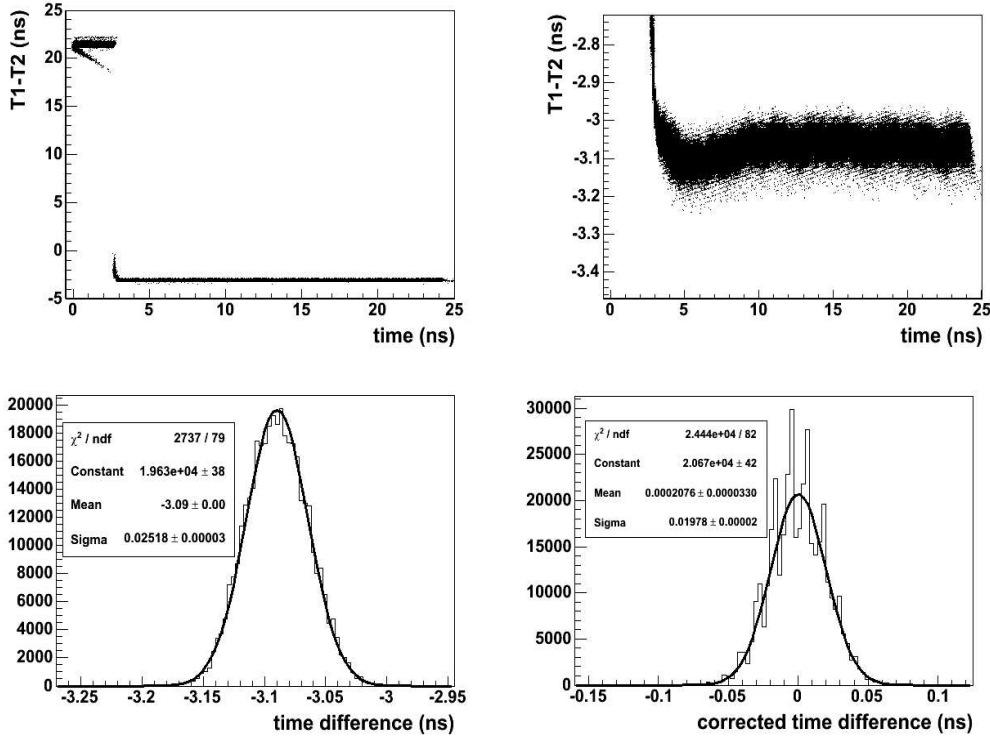


Figure 3.15: Top: Stability of the time difference of the TAQUILA+FEE system versus the clocking cycle. right panel is a zoom of this distribution. We can see the slightly non-linear behaviour. Bottom-left: Projected time difference between both channels between 5 and 10 ns. Bottom-right: Projected time difference after correction in the same range. The width of the gaussian fit gives the time resolution.

corresponds to the implementation of a constant fraction in software ( $\sigma < 10$  ps). The resolution of the method is  $\sigma = 9.6$  ps, thus the intrinsic time resolution obtained for the plastic and PMT is  $\approx 12.8$  ps. The difference between this result and the results achieved with modular electronics ( $\sigma \approx 8$  ps) might be due to different high voltages applied in the phototubes or different intensities of the laser used, as well as the amplitude resolution of the oscilloscope. This method is therefore very appropriate to achieve the time resolutions required.

From these two methods, we can estimate that the intrinsic time resolution of scintillators and PMTs is around 10 ps ( $\sigma$ ).

It should be taken into account the fact that these data correspond to a UV laser and a relatively small scintillator, so all the pulses have the same

amplitude and shape. In order to obtain more realistic results, some tests with particle beams or cosmic rays should be performed.

One of the main drawbacks of this readout method is the very high cost per channel. This readout is only affordable for systems with a relatively small number of channels.

Results obtained with the TAQUILA card, are very good ( $\sigma \approx 20$  ps). They are not as good as the best resolution obtained from pulse shape analysis. The main advantage of this readout method is that it is much cheaper, and therefore, more appropriate for detectors with a large number of electronic channels. Comparing this time resolution with the ones achieved with other read-out RPC electronics, such as the one developed for ALICE experiment, this values are better than the the resolution measured ( $\sigma_{TDC} = 20$  ps [31] and  $\sigma_{FEE\&cables} \sim 12$  ps), although ALICE results correspond to a real test with the beam). In our case, we have only tested two channels with a time calibrator. These results obtained have shown that this electronics is suitable for our high resolution time measurements. Again, this test allows only to obtain the intrinsic resolution of the electronics. If we want to measure the time resolution which can be achieved, a test beam with detectors should be performed, but the results obtained are very encouraging.

# Chapter 4

## Conceptual Design

In this chapter, the design of a high resolution time-of-flight wall for charged particles and ions is proposed as a part of the  $R^3B$  detection system.

According with the requirements discussed in section 1.3, we present two possible alternatives for the construction of the ToF wall: Resistive Plate Chambers (RPCs) and Scintillators coupled to fast photomultiplier tubes.

### 4.1 Design concepts

#### 4.1.1 RPCs

As mentioned in chapter 2, RPCs have been used to construct large area time of flight detectors, reaching time resolutions of the order of  $\sigma_{ToF} < 60$  ps. However, most of the designed RPCs are used with minimum ionizing particles [2, 27, 28], and very little information is available about the response of these detectors with heavy ions [29].

#### Geometry

The design of a large area ToF wall made of three detection planes rotated  $120^\circ$  one respect to the other is proposed (Fig. 4.1-left). Each plane will consist on 8 modules according to the geometry shown in figure 4.1-right. There are 6 horizontal modules and the last two are placed vertically in order to cover the 1.5 m diameter surface corresponding to the acceptance of fission fragments flying at 600 MeV/u (Sect. 1.3.3). The surface covered by the three detection planes is higher than 99% of full acceptance for 600 MeV/u beams (Fig. 4.2). Every plane presents a segmented readout system in order to determine the position.

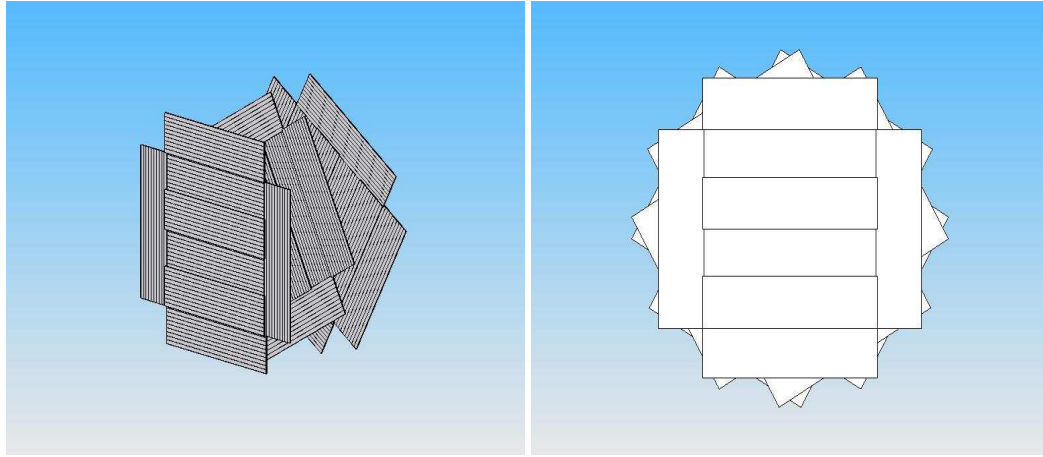


Figure 4.1: Schematic representation of the design proposed for the ToF wall. The left panel shows the three detection planes. The right panel represents the proposed geometry for the 8 RPC modules that constitute each plane.

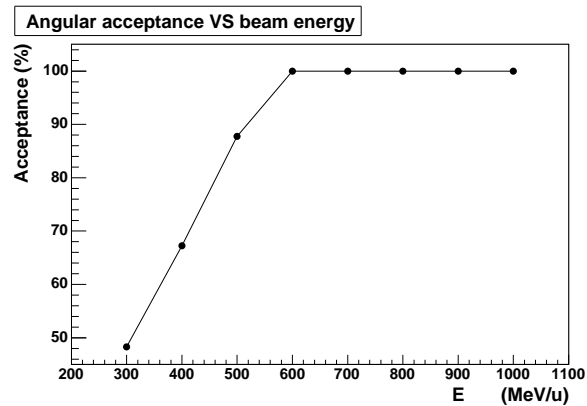
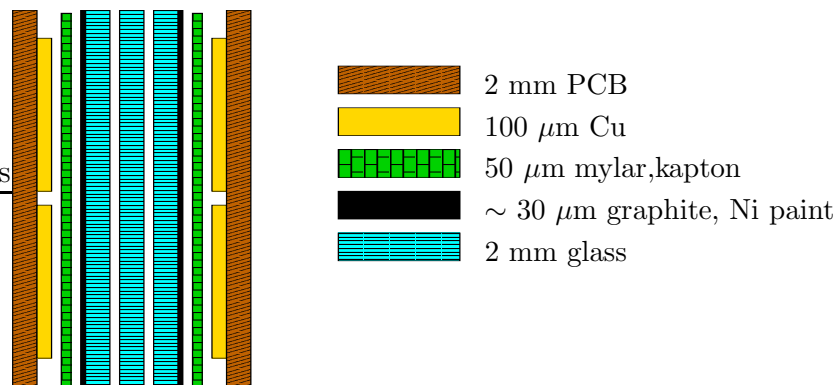


Figure 4.2: Angular acceptance of the RPC wall covered by the three detection planes for different energies of the beam. The full acceptance is achieved for energies larger than 600 MeV/u.

This multilayer design allows also to reduce the obtained time resolution with a single layer detector by a factor  $\sqrt{3}$ , provided that particle has produced signals in all the layers. Assuming a time resolution of 50 ps ( $\sigma$ ) per plane, the resulting time resolution expected is therefore of the order of  $\sigma_{ToF} = 50/\sqrt{3} \approx 30$  ps.

## RPC modules

As mentioned before, each detection plane will be constituted by eight modules. Every module would be a 2-gap resistive plate chamber with a dimension of  $100 \times 26 \text{ cm}^2$ . In principle, a stack of three glass plates (2 mm thick each) is considered, spaced one from the other with nylon fishing line with a diameter of  $300 \mu\text{m}$ , creating two different gas gaps. The gas gaps will be filled with the standard mixture (see section 2.1.2). The outer surfaces of the two outer glass plates will be in contact with a conductive layer acting as electrodes (graphite or nickel paint have been considered). A differential high voltage to produce an electric field of typically  $100 \text{ kV/cm}$  will be applied to the electrodes. Then a mylar or kapton foil will isolate them from the readout system. This system consists on two printed circuit board plates (around 2 mm thick) surrounding the stack of glass plates. These plates will have copper pick-up strips in the inner surfaces. The PCB plates, will also constitute the main frame of each RPC module. A cross section of the design is shown in figure 4.3.



*Figure 4.3: A cross section (not to scale) of one RPC module is shown with the three inner glass plates surrounded by the electrodes, the mylar foils and the PCB plates with the copper strips acting as signal pick up system.*

Energy losses per detector module have been calculated using AMADEUS for different charges and energies of the fragments as well as energy deposited in the gas gaps in order to evaluate the minimum energy and charge that will be detected by the ToF wall (See figure 4.4). From the results obtained, we can conclude that fragments heavier than  $^{208}\text{Pb}$  at energies around  $500 \text{ MeV/u}$  will not traverse all the planes of the ToF wall at energies around and below  $500 \text{ MeV/u}$ . Lighter elements will traverse all the detection planes, and the energy deposited in gas will be of the order of MeV, except for those

lighter than  $^{12}\text{C}$ . The energy deposited in the gas by these fragments is some keV, therefore it is enough to produce ionizations in gas.

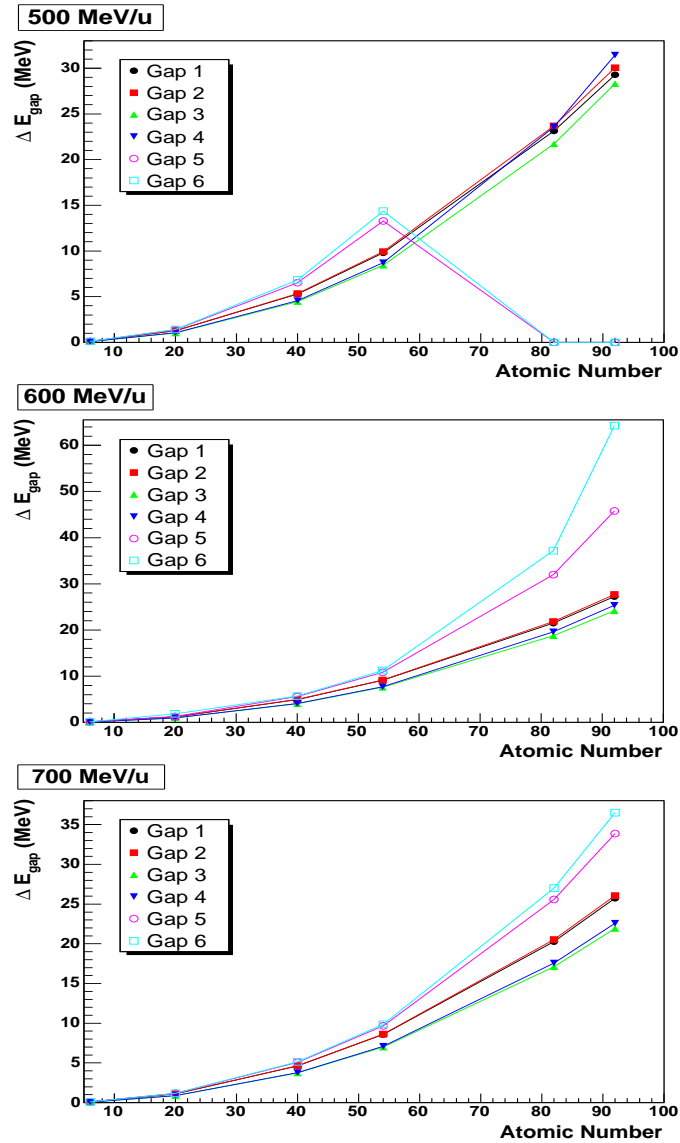
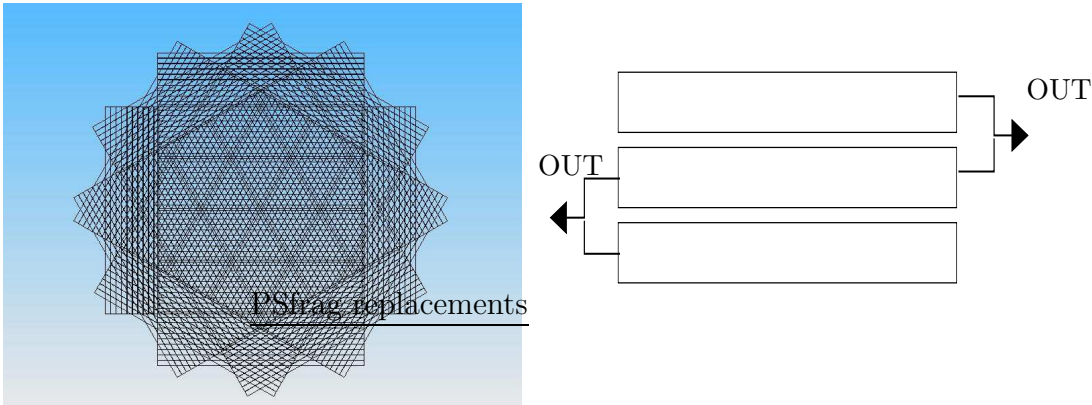


Figure 4.4: Energy deposited per gas gap in the ToF wall for different charges and energies of the beam. Elements heavier than  $^{208}\text{Pb}$  at 500 MeV/u will not traverse all the planes (top panel).

## Readout system and electronics

At the moment we are considering the segmentation within each module with 10 copper strips per module ( $100 \times 2.5 \text{ cm}^2$ ) with 1 mm gap between them. Anode and cathode strips will provide a differential signal. The signals induced by charged particles will be taken from both sides of the RPC module, determining the position along the 1 m length with a resolution better than 3 mm (see sect. 1.4). This segmented readout strips configuration provides individual detection cells with a surface of about  $12 \text{ cm}^2$  (Fig. 4.5-left), minimizing the multihit probability. The probability of multihit is below 1% for fission fragments at 600 MeV/u and better than 7% even for multifragmentation reactions (5 fragments). The position information would also help to correct the time of flight with a better definition of the pathlength, improving the final time resolution. In order to reduce the number of electronic channels without losing resolution in position, the signals induced in two consecutive strips could be read by the same amplifier and disentangled later by comparing both sides of the fired strips (Fig. 4.5-right).



*Figure 4.5: Left: Front view of the ToF wall detector with individual detection cells defined by the geometry of the pickup strips. Right: Readout scheme of the pickup strips.*

For the read-out electronics the TAQUILA [2] front end electronics and readout system is considered. This electronics allows the measurement of time and charge of the signals induced in the pickup electrodes. The intrinsic resolution of this electronics is around 20 ps, fulfilling our requirements (see section 3.3 for details).

### 4.1.2 Plastic scintillators

As an alternative, we propose a ToF wall based in the use of standard organic scintillators coupled to fast photomultipliers (PMT). In order to achieve a time resolution below 60 ps we consider individual counters made of organic scintillator material with a dimension of  $6 \times 150 \text{ cm}^2$  and a thickness of 5 mm. With this dimensions we will need 30 paddles with 1 cm overlap to cover the  $1.5 \text{ m}^2$  total surface. As in the RPC design we will have multiple layers (two instead of three) disposed in a perpendicular configuration, being a total number of 60 paddles (Fig. 4.6). These scintillator paddles will be equipped with 120 light guides, photomultipliers and electronic channels. The acceptance of this design is almost 100% for energies higher than 600 MeV/u, and the multihit probability considering  $36 \text{ cm}^2$  individual detection cells is lower than 1% for fission fragments and around 14% in multifragmentation reactions (5 fragments).

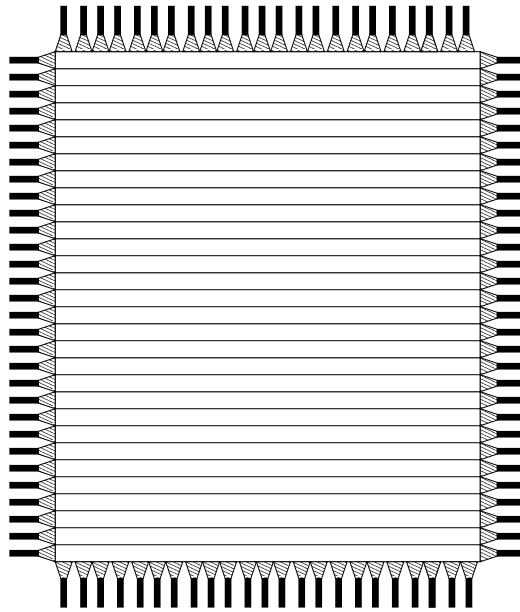


Figure 4.6: Front view of the ToF wall detector based on scintillators.

Energy deposited in the scintillator material has also been calculated using AMADEUS for different charges and energies of the fragments to evaluate the minimum energy and charge that will be detected by the ToF wall (See figure 4.7). From these results, we see that all elements, from  $^{12}\text{C}$  to those heavier than  $^{208}\text{Pb}$  at energies around 500 MeV/u will traverse both planes of the ToF wall at energies around 500 MeV/u. The energy deposited in the plastic by this fragments ranges from thousands to hundreds of MeV,

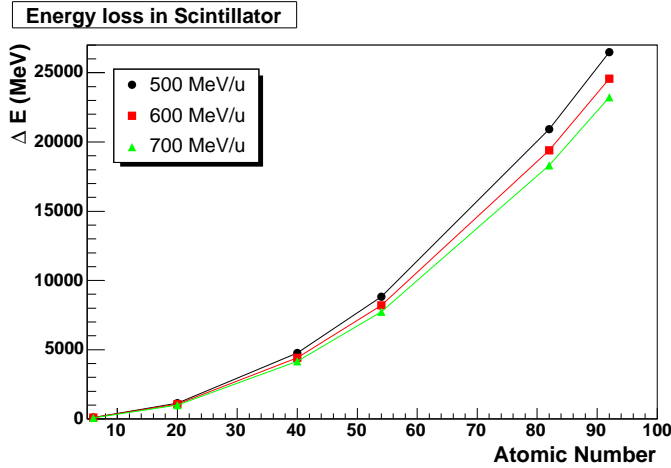


Figure 4.7: Front view of the ToF wall detector based on scintillators. Right: Readout scheme of the pickup strips.

therefore is enough to produce scintillation.

As far as the time resolution is concerned, the total time resolution achieved with this type of detectors is around 75 ps per layer for fission fragments [9]. Therefore the expected time resolution is around  $\sigma_{ToF} = 75/\sqrt{2} \approx 53$  ps.

The use of Bicron BC420 as scintillation material coupled to Hamamatsu H2431 tubes is considered. As in the RPC case, signals will be taken from both extremes of the scintillator. For the readout we propose the same solution as for the RPC, although, in this case, the front end electronics board should be adapted to the PMT signals.

## 4.2 Cost estimate

In this section, the cost estimate of both designs proposed is presented.

### 4.2.1 RPCs

The cost estimate of such a ToF wall based on the concept described above is presented in table 4.1. This estimation was obtained assuming a three layer ToF wall made of eight RPC modules each, with 10 readout pads and collecting the signals from both extremes of the pads and reading the signals of two consecutive strips with the same preamplifier. Then, 10 electronic channels per module are needed, 80 channels per layer and a total number of 243 channels. This number is due to the fact that readout strips

are connected according to figure 4.5-right. Housing and holding entry corresponds to the design and construction of a mechanical structure for the detector. Gas system entry corresponds to the set of devices which allow to control gas flow and mixture percentages in RPCs. Power supply is related with the high voltage needed for the RPC to work. Cost estimation of it is based on the price of standard high voltage power supplies. Electronics cost estimate is based in the 200 euro per channel cost of the FEE+TAQUILA. DAQ entry corresponds to the data acquisition system. The accuracy in the estimation is of the order of 20 %.

Item	cost (Keuro)
R&D+Prototypes	30
RPC materials	20
RPC housing & holding	30
Gas system	30
Power Supply	20
Electronics (243 ch.)	50
DAQ(SAM3+RIO3+crate)	35
<b>Total</b>	<b>215</b>

Table 4.1: Cost estimate for a three layer ToF wall based on RPCs

## 4.2.2 Plastic scintillators

The cost estimate for this option is presented in table 4.2. This estimation is based on the use of 30 horizontal and 30 vertical detectors equipped with 120 PMTs and electronic channels. The estimation of the electronics cost is based again in the use of FEE+TAQUILA option.

As we can see, the cost of an RPC based ToF wall versus a scintillator based one is a factor two cheaper. This is one of the reasons of using RPCs instead of plastic scintillators. The cost is cheaper and the performances are almost the same.

---

Item	cost (Keuro)
R&D+Prototypes	30
1.5×1.5 m <sup>2</sup> BC420	10
Light guides	10
120 Hamamatsu 2431 PMTs	276
Mechanics	15
Power supply	50
Electronics (120 ch.)	24
DAQ(SAM3+RIO3+crate)	35
<b>Total</b>	<b>450</b>

---

Table 4.2: Cost estimate for a two layer ToF wall based on scintillators



# Conclusions

The goal of this work was to define the performances of a ToF wall detector for heavy ion identification, discuss the present technologies available to achieve these requirements and propose a conceptual design based on the previous considerations.

This detector will be used to measure the time of flight in order to obtain the velocities of the fragments coming out from the nuclear reactions induced by relativistic heavy ions at the  $R^3B$  experiment, that will take place at the new FAIR facility in Darmstadt (Germany).

The main requirements are to cover the full acceptance of all the outgoing reaction products and to isotopically identify them up to the mass 200. The possibility of multihit-event identification has also been considered. According to these requirements the most appropriate features are the following:

**ToF resolution:** The time accuracy needed to separate masses around  $A \sim 200$  at 700 MeV/u is around  $\Delta T_{oF}/T_{oF} \approx 7 \times 10^{-4}$ , for 15 m path-length this value  $\sigma_{T_{oF}} \approx 20$  ps, therefore this path-length seems reasonable for the nowadays timing technology.

**Position and surface:** As far as size is concerned, the one required to cover the full acceptance for fission fragments at 500 MeV/u at 15 m from the target is  $1.5 \times 1.5$  m<sup>2</sup>.

**Granularity:** In order to make possible multi-hit event identification, the detector will be divided in strips of 2.5 cm, providing a multihit probability of double hits lower than 7% for multifragmentation reactions (5 fragments).

The START will be given by a CVD diamond detector. Due to the fact that diamond detectors' intrinsic time resolution is  $\sigma = 29$  ps, the resolution will be limited by this value. Other possible detectors should be considered as START in order to avoid this limitation.

Two different technologies have been considered to implement such a detector: Resistive Plate Chambers (RPC), or fast plastic scintillators coupled to fast photomultiplier tubes.

Resistive Plate Chambers and scintillator detectors are very suitable devices for time-of-flight measurements. The efficiency and time resolution achieved with the ‘state of the art’ timing RPCs, multigap glass RPCs in a range of 0.2-0.3 mm gap width, is about 99% and 50 ps ( $\sigma$ ) respectively for MIPS. Very little is known about the behaviour of RPCs with heavy ions. Further studies should be performed in order to check the performance of RPCs with them, but these results are very encouraging for the use of these type of detectors in the identification of heavy ions by time of flight measurements, as an alternative to the standard scintillation detectors. Scintillators have shown excellent performances for new scintillation materials and photomultiplier technologies (better than 10 ps ( $\sigma$ ) for small scintillators and heavy ions, around 75 ps( $\sigma$ ) for 1m scintillatos and fission fragments ).

Different readout methods for the signals have been tested: standard modular electronics, pulse shape analysis and the new TAQUILA electronics developed for FOPI the RPCs.

The time resolution obtained with modular electronics is very good. Electronics resolution is  $\sigma_{elec} \approx 8$  ps and the intrinsic resolution of plastic scintillator combined with the PMTs depends on two factors, the high voltage applied and the light output, e.g. at very high voltages the time resolution deteriorates. The second factor is related with the fact that time resolution in scintillation detectors improves with the number of photoelectrons. From pulse shape analysis of the scintillators signals, we have shown that the time resolution achievable depends on the parameter chosen to define the time, ranging from 300 to 16 ps. The best result obtained in this case corresponds to the implementation of a constant fraction in software. The intrinsic resolution of the method has been measured with a pulser, obtaining  $\sigma = 9.6$  ps, thus the intrinsic time resolution of the plastic and PMT is  $\approx 12.8$  ps. The difference between this result and the results achieved with modular electronics ( $\sigma \sim 8$  ps) might be due to different high voltages applied in the phototubes or different intensities of the laser used, as well as the amplitude resolution of the oscilloscope. This method is therefore very appropriate to achieve the time resolutions required.

It should be taken into account the fact that these data correspond to a UV laser and a relatively small scintillator, thus all the pulses have the same amplitude and shape. In order to obtain more realistic results, some tests with particle beams or cosmic rays should be performed.

One of the main drawbacks of this readout method is the very high cost per channel. This readout is only affordable for systems with a relatively

small number of channels.

The results obtained with integrated electronics (TAQUILA card), are very good ( $\sigma \approx 20$  ps). They are not as good as the best resolution obtained from pulse shape analysis. The main advantage of this readout method is that it is much cheaper, and therefore, more appropriate for detectors with a large number of electronic channels. The results obtained have shown that this electronics is suitable for our high resolution time measurements. Comparing this time resolution with the one achieved with other read-out RPC electronics, such as the one developed for ALICE experiment, this values are better than the the resolution measured ( $\sigma_{TDC} = 20$  ps [31] and  $\sigma_{FEE\&cables} \sim 12$  ps), although ALICE results correspond to a real test with the beam). In our case, we have only tested two channels with a time calibrator. Again, this test allows only to obtain the intrinsic resolution. If we want to measure the real time resolution that can be achieved, a test beam with detectors should be performed, but the results obtained are very encouraging.

Finally, a large area ToF wall based on RPC detectors has been proposed. It consists on three detection planes rotated  $120^\circ$  one respect to the other. Each plane will consist on 8 modules. Every module will be a multigap resistive plate chamber with a dimension of  $100 \times 26$  cm<sup>2</sup> with a segmented anode design. In principle, a stack of three gas plates is considered, spaced one from the other with nylon fishing line with a diameter of  $300 \mu\text{m}$ , creating two different gas gaps. The outer surfaces of the two outer glass plates will be in contact with a conductive layer acting as electrodes (graphite or nickel paint have been considered). Then a mylar foil will isolate them. The readout system consist on two printed circuit board plates surrounding the stack of glass plates. These plates will have copper pick-up strips in the inner surfaces. At the moment we are considering 10 strips ( $100 \times 2.5$  cm<sup>2</sup>) with 1 mm gap between them, in order to pick up both anode and cathode signals. A differential high voltage will be applied to the electrodes. For the readout, a differential signal will be obtained from anode and cathode pick up strips. In order to reduce the number of electronic channels, the signals induced in two consecutive strips could be read by the same amplifier, So the stripsize is equivalent to a 5 cm one.

This design covers the required surface with 1.5 m diameter. In addition, it will allow to reduce the achievable time resolution with a single layer detector by a factor  $\sqrt{3}$ , resulting in a expected resolution of the order of  $\sigma_{ToF} = 30$  ps. This configuration also provides individual detection cells with a surface of about 12 cm<sup>2</sup>, minimizing the multihit probability. The signals induced by charged particles will be taken from both sides of the RPC module. These two measurements will allow to determine the position along

the 1 m length of the detector by the time difference method. In addition, this position information will help to correct the time-of-flight, improving the time resolution. For the read-out electronics the TAQUILA front end electronics and readout system is considered.

# Conclusiones

En este trabajo se ha pretendido definir los requisitos de un muro detector de tiempo de vuelo para la identificación de iones pesados, discutir las diferentes tecnologías disponibles actualmente para satisfacer estas necesidades, así como proponer un diseño basado en las consideraciones anteriores.

Este detector se usará para la medida del tiempo de vuelo de los fragmentos procedentes de las reacciones nucleares producidas por iones pesados a energías relativistas en el experimento  $R^3B$ , que tendrá lugar en las nuevas instalaciones de FAIR en Darmstadt (Alemania).

Los requisitos principales que tiene que cumplir este detector son cubrir toda la aceptación de los productos de las reacciones y separarlos hasta la masa 200. La posibilidad de identificar sucesos con impactos múltiples también se ha tenido en cuenta, lo que va a determinar la granularidad de nuestro detector. De acuerdo con estos requisitos, las características más apropiadas son las siguientes:

**Resolución temporal:** la resolución necesaria para separar masas en torno a  $A \sim 200$  a  $700$  MeV/u es aproximadamente  $\Delta ToF/ToF \approx 7 \times 10^{-4}$ , que para una distancia de 15 m entre los detectores se traduce en una resolución absoluta de  $\sigma_{ToF} \approx 20$  ps. Por tanto, esta distancia parece razonable dada la tecnología actual en cuestión de medida de tiempos.

**Posición y superficie:** en lo referente al tamaño, el necesario para cubrir toda la aceptación de los fragmentos de fisión a 500 MeV/u a una distancia de 15 m desde el blanco es de 1,5 m de diámetro. Debido a la fuerte focalización hacia adelante de los productos a energías relativistas, energías mayores requieren una menor superficie, por lo que la aceptación total está garantizada para energías superiores del haz.

**Granularidad:** Para posibilitar la identificación de sucesos con impactos múltiples, el detector deberá estar dividido en tiras de 2,5 cm de ancho, proporcionando una probabilidad de impactos dobles inferior al 7% para reacciones en las que se han producido 5 fragmentos.

El START vendrá dado por un detector de diamante. Puesto que la resolución temporal intrínseca de este tipo de detectores es  $\sigma = 29$  ps, la resolución total estará limitada por este valor, por tanto, se podría tener en cuenta el uso de otro tipo de dispositivos para evitar esta limitación. Para el STOP, se han considerado las dos tecnologías más utilizadas actualmente cámaras de placas resistivas (RPCs) y centelleadores rápidos acoplados a tubos fotomultiplicadores (PMTs) también rápidos. Ambos tipos de detectores son adecuados para medidas de tiempo de vuelo de gran precisión. La eficiencia y la resolución temporal alcanzadas actualmente con RPCs es del 99% y 50 ps ( $\sigma$ ), respectivamente con partículas mínimamente ionizantes (MIPs).

Actualmente se sabe muy poco acerca del comportamiento de las RPCs con iones pesados y deberían realizarse estudios para comprobar las prestaciones de este tipo de detectores con ellos, como alternativa a los detectores de centelleo usados normalmente.

El desarrollo de centelleadores rápidos junto con la evolución de los fotomultiplicadores ha permitido alcanzar resoluciones temporales excelentes (menor de 10 ps ( $\sigma$ ) para centelleadores pequeños y en torno a 75 ps( $\sigma$ ) para centelleadores de 1 m y fragmentos de fisión).

Para la lectura de las señales producidas por ambos tipos de detectores, se han probado tres métodos diferentes: la electrónica modular utilizada normalmente, la digitalización completa de las señales producidas para su posterior análisis mediante *software* y la tarjeta digitalizadora (TAQUILA) desarrollada para las RPCs del experimento FOPI.

La resolución temporal obtenida con electrónica modular es  $\sigma_{elec} \approx 8$  ps, mientras que la resolución temporal de los centelleadores y los PMTs depende principalmente de dos factores: la tensión aplicada y la luz producida en el plástico. Por ejemplo, para voltajes muy altos en el PMT, la aparición de ruido deteriora la resolución temporal. La intensidad de la luz está relacionada con el hecho de que en los detectores de centelleo, la resolución mejora con el número de fotoelectrones emitidos.

Del análisis del pulso digitalizado, se ha obtenido que la resolución alcanzada depende del parámetro escogido para definir el tiempo, y los valores varían entre los 300 ps y los 16 ps ( $\sigma$ ). Este último resultado se ha obtenido con la implementación de un *Constant Fraction Discriminator* por software. La resolución intrínseca del método se ha medido con un generador de pulsos y es  $\sigma \approx 9.6$  ps, por tanto la resolución intrínseca del sistema plástico+PMT es  $\sigma \sim 12,8$  ps. La diferencia entre este resultado y el obtenido con electrónica modular ( $\sigma \sim 8$  ps) puede ser debida a que los voltajes aplicados en los tubos o la intensidad del láser utilizado para excitar el plástico eran diferentes, así como la resolución en amplitud del osciloscopio. El uso de este método parece por tanto adecuado para obtener las resoluciones

requeridas. Debe tenerse en cuenta el hecho de que los datos analizados corresponden a un láser UV y a centelleadores relativamente pequeños. Como consecuencia, todos los pulsos tienen la misma forma y amplitud y la atenuación de la luz en el seno del centelleador no es significativa. Para obtener resultados más realistas, deberían hacerse medidas con haces de partículas o rayos cósmicos.

Los resultados obtenidos con TAQUILA son muy buenos ( $\sigma \approx 20$  ps), aunque no tan buenos como los obtenidos por los dos métodos anteriores. La ventaja principal de este método es que es mucho más barato, y por tanto más apropiado para detectores con varios cientos de canales de electrónica. Los resultados obtenidos muestran que este tipo de electrónica es adecuada para nuestras medidas de tiempo. Comparando esta resolución temporal con la alcanzada por otras electrónicas desarrolladas para RPCs, como por ejemplo la de ALICE ( $\sigma_{TDC} = 20$  ps y  $\sigma_{FEE\&cables} \sim 12$  ps), los resultados obtenidos con TAQUILA son mejores, aunque debe tenerse en cuenta que los resultados de ALICE se corresponden con un test real, mientras que en nuestro caso sólo se han probado 2 canales con un calibrador de tiempos.

Finalmente, se ha propuesto el diseño de un muro de tiempo de vuelo basado en RPCs. Este muro está formado por tres planos iguales rotados  $120^\circ$  uno respecto de otro. Cada plano está constituido por 8 módulos. Cada uno de los módulos es una RPC *multigap* de  $100 \times 26$  cm<sup>2</sup>. Este diseño cubre la superficie requerida de 1.5 m de diámetro con una aceptación superior al 99% para la superficie común a los tres planos. Además, permite reducir la resolución temporal en un factor  $\sqrt{3}$  si se ha producido señal en los tres planos, obteniendo una resolución temporal de  $\sigma_{ToF} = 30$  ps. Esta configuración proporciona además celdas de detección con una superficie de 15 cm<sup>2</sup> aproximadamente, minimizando así la probabilidad de impactos múltiples. La señal inducida en los electrodos de lectura es recogida a ambos lados del módulo. Estas dos medidas permiten determinar la posición a lo largo del módulo con una precisión de aproximadamente 2 mm, pudiendo así corregir la medida de tiempo de vuelo por la longitud recorrida. Para la electrónica de lectura se considera el uso de la TAQUILA.



# Appendix A

## Relation between resolution in bending angle and position resolution of tracking detectors

We will derive here the expression which relates the resolution in the measurement of the bending angle and the position resolution in tracking detectors.

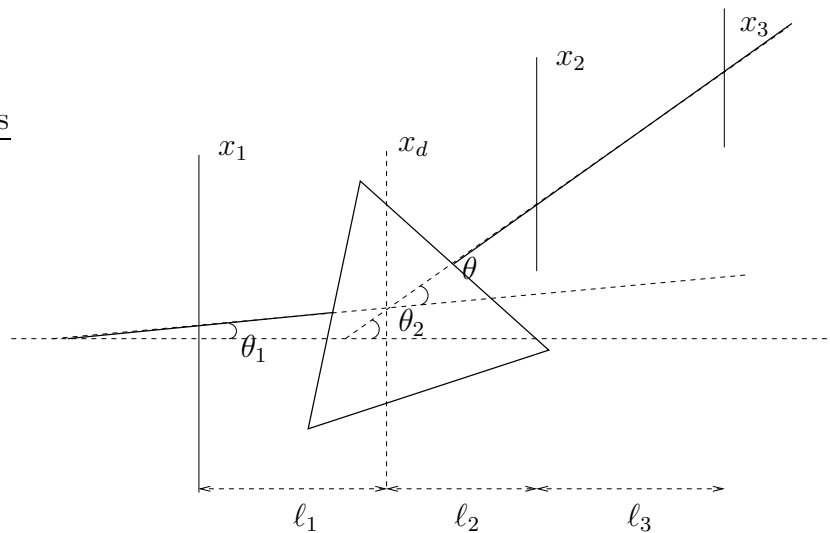


Figure A.1: Relation between bending angle and position detectors.

From Fig. A.1 the angles are defined as

$$\theta_2 \approx \tan \theta_2 = \frac{x_3 - x_2}{\ell_3} = \frac{x_2 - x_d}{\ell_2} \quad (\text{A.1})$$

$$\theta_1 \approx \frac{x_d - x_1}{\ell_1} \quad (\text{A.2})$$

$$\theta = \theta_2 - \theta_1 \quad (\text{A.3})$$

From eq. (A.1) we get

$$x_d = x_2 - \ell_2 \theta_2 \quad (\text{A.4})$$

Using this result in eq. (A.2) and substituting in (A.3) we obtain

$$\theta = \theta_2 - \frac{x_2 - \ell_2 \theta_2 - x_1}{\ell_1} = \left(1 + \frac{\ell_2}{\ell_1}\right) \theta_2 - \frac{x_2 - x_1}{\ell_1} \quad (\text{A.5})$$

Substituting  $\theta_2$  from (A.1) and reordering terms we get

$$\theta = \frac{x_1}{\ell_1} - \left(\frac{1}{\ell_3} + \frac{\ell_2}{\ell_1 \ell_3} + \frac{1}{\ell_1}\right) x_2 + \left(1 + \frac{\ell_2}{\ell_1}\right) \frac{x_3}{\ell_3} \quad (\text{A.6})$$

Assuming  $\ell_1 = \ell_2 = \ell_3 = \ell$ , eq. (A.6) can be simplified even more obtaining

$$\theta = \frac{1}{\ell} (x_1 + 3x_2 + 2x_3) \quad (\text{A.7})$$

Finally from (A.7), is easy to obtain

$$\Delta\theta = \frac{1}{\ell} \sqrt{(\Delta x_1)^2 + (3\Delta x_2)^2 + (2\Delta x_3)^2} \quad (\text{A.8})$$

# Appendix B

## Simulation codes

### B.1 Estimation of multihit probability in fission

```
Double_t dist = 15; //distance for the detector (m)
E_beam=.7; //GeV
//Int_t stripsize=3; //cm
beamspot=0; //cm
cout << "Calculation of fission kinematics for uranium" <<endl;
//cout << "please insert the energy of the beam (GeV/u):";
//cin >>E_beam;
//cout << "please insert the size of the strip (cm):";
//cin >>stripsize;
cout << " Energy of the beam "<< E_beam <<" GeV/u"<<endl;

//Lorentz boost in z axis to LAB frame
beta[0] = 0;
beta[1] = 0;
beta[2] = sqrt(1-(1/pow((E_beam/uma+1),2)));
Double_t aux = sqrt(pow(beta[0],2)+pow(beta[1],2)+pow(beta[2],2));
gamma = pow((1-aux*aux),-0.5);
cout << " Beam velocity (beta) \t"<< aux <<"c"<< endl;
cout << " Lorentz factor (gamma) \t"<< gamma << endl;
for( k=0;k<100000;k++){
    //flag=0;
    Double_t phi0 = q.Rndm(1)*2*pi;
    Double_t costheta0 = 1-2*q.Rndm();
    Double_t theta0 =acos(costheta0);
    Double_t r=beamspot*q.Rndm();
    pos0[0]=r*sin(theta0)*cos(phi0);
```

```

pos0[1]=r*sin(theta0)*sin(phi0);
pos0[2]=0;
Z1= 20+q.Integer(37);
Z2 = 92 - Z1;
N1 = 146./92.*Z1;
N2 = 146-N1;
A1 = Z1+N1;
A2 = Z2+N2;
//Total Kinetic energy (Wilkins model)(GeV)
TKE = (0.00144*Z1*Z2)/(1.16*(pow(A1,1./3.)*(1.+2./3.*0.6)+
      pow(A2,1./3.)*(1.+2./3.*0.6))+2);
//Velocities moduli of the fragments in CM frame (cm/ns)
Double_t v11 = sqrt(2*A2*TKE/(uma*A1*(A1+A2)))*c;
Double_t v22 = v11*A1/A2;
//Maximum polar angle and azimuth = 0
Double_t phi = q.Rndm()*2*pi;
Double_t costheta = 1-2*q.Rndm();
Double_t theta =acos(costheta);
//Fragment 1
v1_cm[0] = v11*sin(theta)*cos(phi);
v1_cm[1] = v11*sin(theta)*sin(phi);
v1_cm[2] = v11*cos(theta);
//Fragment 2
v2_cm[0] = v22*sin(pi-theta)*cos(phi+pi);
v2_cm[1] = v22*sin(pi-theta)*sin(phi+pi);
v2_cm[2] = v22*cos(pi-theta);
//LAB frame

//*****velocities*****
//Fragment 1
v1_lab[0] = v1_cm[0]/(gamma*(1+beta[2]*v1_cm[2]/c));
v1_lab[1] = v1_cm[1]/(gamma*(1+beta[2]*v1_cm[2]/c));
v1_lab[2] = (v1_cm[2]+beta[2]*c)/(1+beta[2]*v1_cm[2]/c);
//Fragment 2
v2_lab[0] = v2_cm[0]/(gamma*(1+beta[2]*v2_cm[2]/c));
v2_lab[1] = v2_cm[1]/(gamma*(1+beta[2]*v2_cm[2]/c));
v2_lab[2] = (v2_cm[2]+beta[2]*c)/(1+beta[2]*v2_cm[2]/c);

//*****Positions*****
tof1=1500/v1_lab[2];
tof2=1500/v2_lab[2];
//Fragment 1
pos1[0] = pos0[0]+v1_lab[0]*tof1;

```

```

pos1[1] = pos0[1]+v1_lab[1]*tof1;
pos1[2] = pos0[2]+v1_lab[2]*tof1;
XY_dist.Fill(pos1[0],pos1[1]);
//Fragment 2
pos2[0] =pos0[0]+ v2_lab[0]*tof2;
pos2[1] =pos0[1]+v2_lab[1]*tof2;
pos2[2] =pos0[2]+ v2_lab[2]*tof2;
separation = sqrt(pow(pos2[0]-pos1[0],2)+pow(pos2[1]-pos1[1],2));
XY_dist.Fill(pos2[0],pos2[1]);
for(m=0;m<4;m++)
{
flag=0;
if(fabs(pos2[1]-pos1[1])<=stripsize[m]){
MultihitX[m]++;
flag++;
}
if(fabs(pos2[0]-pos1[0])<=stripsize[m]){
MultihitY[m]++;
flag++;
}
if(flag==2){
Multihit[m]++;
cout<<"*";
}
if(separation<=stripsize[m])
Multihit2[m]++;
}
}
for(l=0;l<4;l++)
{
cout<<"\n Size of the strips:"<<stripsize[l]<<"cm"<<endl;
cout<<"*****"<<endl;
cout<<" Number of events: "<<k<< endl;
cout<<"Number of multiple hits X: "<<MultihitX[l]<< endl;
cout<<"Number of multiple hits Y: "<<MultihitY[l]<< endl;
cout<<"Number of multiple hits (X&Y): "<<Multihit[l]<< endl;
cout<<"Number of multiple hits (distance): "<<Multihit2[l]<< endl;
Double_t ProbX=Double_t(MultihitX[l])/Double_t(k);
Double_t ProbY=Double_t(MultihitY[l])/Double_t(k);
Double_t Prob=Double_t(Multihit[l])/Double_t(k);
Double_t Prob2=Double_t(Multihit2[l])/Double_t(k);
cout<<"Probability of Multihit X: " <<ProbX*100<<"%"<<endl;
cout<<"Probability of Multihit Y: " <<ProbY*100<<"%"<<endl;
}
}

```

```

cout<<"Probability of Multihit (X&Y): " <<Prob*100<<"%"<<endl;
cout<<"Probability of Multihit (distance): " <<Prob*100<<"%"<<endl;
}
cout<<"DONE"<<endl;
TCanvas win("win","in",2);
win.cd(1);
XY_dist.Draw("ZCOL");

}

```

## B.2 Estimation of multihit probability in multifragmentation

```

Double_t pi=TMath::Pi(); //pi
//Beam Properties
Double_t E_beam,beta[3],gamma;
//Fragment 1
Double_t Z1,A1,v1_cm[3],v1_lab[3],pos1[3],tof1;
//Fragment *
Double_t Zstar,Astar,vstar_cm[3];
//Fragment 2
Double_t Z2,A2,v2_cm[3],v2_lab[3],pos2[3],tof2;
//Fragment **
Double_t Z2star,A2star,v2star_cm[3];
//Fragment 3
Double_t Z3,A3,v3_cm[3],v3_lab[3],pos3[3],tof3;
//Fragment ***
Double_t Z3star,A3star,v3star_cm[3];
//Fragment 4
Double_t Z4,A4,v4_cm[3],v4_lab[3],pos4[3],tof4;
//Fragment 5
Double_t Z5,A5,v5_cm[3],v5_lab[3],pos5[3],tof5;
//Distances Between fragments
Float_t dx12,dy12;
Float_t dx13,dy13;
Float_t dx14,dy14;
Float_t dx15,dy15;
Float_t dx23,dy23;
Float_t dx24,dy24;
Float_t dx25,dy25;
Float_t dx34,dy34;

```

```
Float_t dx35,dy35;
Float_t dx45,dy45;
//Begin of program
cout << "Calculation of multihit probability in multifragmentation
of uranium" <<endl;
cout << "please insert the energy of the beam (GeV/u):";
//cin >>E_beam;
E_beam=600;
cout << "please insert the size of the strip (cm):";
stripsize = 15;

Char_t buffer[23];

cout << "Calculating... Please wait"<<endl;
cout << " Energy of the beam "<< E_beam <<" MeV/u"<<endl;

//Calculation of the beam properties
beta[0] = 0;
beta[1] = 0;
beta[2] = sqrt(1-(1/pow((E_beam/uma+1),2)));
Double_t aux = sqrt(pow(beta[0],2)+pow(beta[1],2)+pow(beta[2],2));
gamma = pow((1-aux*aux),-0.5);

cout << " Beam velocity (beta) \t"<< aux <<"c"<< endl;
cout << " Lorentz factor (gamma) \t"<< gamma << endl;

//LOOP OVER ALL THE NUCLEI
for( k=1;k<=50000;k++){
    //Charges
    Z1=18;
    Zstar=74;
    Z2=18;
    Z2star=56;
    Z3=18;
    Z3star=38;
    Z4=18;
    Z5=20;
    //Masses
    A1=45;
    Astar=193;
    A2=45;
    A2star=148;
    A3=45;
```

```

A3star=103 ;
A4=45;
A5=58;
//Total Kinetic energy (Coulomb Repulsion)(1-->*)
Double_t KE1 = TKE(A1,Z1,Astar,Zstar);
//Total Kinetic energy (Coulomb Repulsion)(2-->**)
Double_t KE2 = TKE(A2,Z2,A2star,Z2star);
//Total Kinetic energy (Coulomb Repulsion)(3-->***)
Double_t KE3 = TKE(A3,Z3,A3star,Z3star);
//Total Kinetic energy (Coulomb Repulsion)(4-->5)
Double_t KE4 = TKE(A4,Z4,A5,Z5);
//Velocities moduli of the fragments in CM frame (cm/ns)
Double_t v11 = sqrt(2*Astar*KE1/(uma*A1*(A1+Astar)))*c;
Double_t vstar = v11*A1/Astar;
Double_t v22 = sqrt(2*A2star*KE2/(uma*A2*(A2+A2star)))*c+vstar/2.;
Double_t v2star = v22*A2/A2star;
Double_t v33 =
sqrt(2*A3star*KE3/(uma*A3*(A3+A3star)))*c+v2star/2.;
Double_t v3star = v33*A3/A3star;
Double_t v44 = sqrt(2*A5*KE3/(uma*A4*(A4+A5)))*c+v3star/2.;
Double_t v55 = v44*A4/A5;
//Random generation of velocity vectors
//Fragment 1
Double_t phi1 = q.Rndm()*2*pi;
Double_t costheta1 = 1-2*q.Rndm();
Double_t theta1 =acos(costheta1);
//Fragment 2
Double_t phi2 = q.Rndm()*2*pi;
Double_t costheta2 = 1-2*q.Rndm();
Double_t theta2 =acos(costheta2);
//Fragment 3
Double_t phi3 = q.Rndm()*2*pi;
Double_t costheta3 = 1-2*q.Rndm();
Double_t theta3 =acos(costheta3);
//Fragment 4
Double_t phi4 = q.Rndm()*2*pi;
Double_t costheta4 = 1-2*q.Rndm();
Double_t theta4 = acos(costheta4);
//Fragment 5
Double_t phi5 = q.Rndm()*2*pi;
Double_t costheta5 = 1-2*q.Rndm();
Double_t theta5 =acos(costheta5);

```

```

//Fragment 1
v1_cm[0] = v11*sin(theta1)*cos(phi1);
v1_cm[1] = v11*sin(theta1)*sin(phi1);
v1_cm[2] = v11*cos(theta1);
//Fragment 2
v2_cm[0] = v22*sin(theta2)*cos(phi2);
v2_cm[1] = v22*sin(theta2)*sin(phi2);
v2_cm[2] = v22*cos(theta2);
//Fragment 3
v3_cm[0] = v33*sin(theta3)*cos(phi3);
v3_cm[1] = v33*sin(theta3)*sin(phi3);
v3_cm[2] = v33*cos(theta3);
//Fragment 4
v4_cm[0] = v44*sin(theta4)*cos(phi4);
v4_cm[1] = v44*sin(theta4)*sin(phi4);
v4_cm[2] = v44*cos(theta4);
//Fragment 5
v5_cm[0] = v55*sin(theta5)*cos(phi5);
v5_cm[1] = v55*sin(theta5)*sin(phi5);
v5_cm[2] = v55*cos(theta5);
//LAB frame

//*****velocities*****
//Fragment 1
v1_lab[0] = v1_cm[0]/(gamma*(1+beta[2]*v1_cm[2]/c));
v1_lab[1] = v1_cm[1]/(gamma*(1+beta[2]*v1_cm[2]/c));
v1_lab[2] = (v1_cm[2]+beta[2]*c)/(1+beta[2]*v1_cm[2]/c);
//Fragment 2
v2_lab[0] = v2_cm[0]/(gamma*(1+beta[2]*v2_cm[2]/c));
v2_lab[1] = v2_cm[1]/(gamma*(1+beta[2]*v2_cm[2]/c));
v2_lab[2] = (v2_cm[2]+beta[2]*c)/(1+beta[2]*v2_cm[2]/c);
//Fragment 3
v3_lab[0] = v3_cm[0]/(gamma*(1+beta[2]*v3_cm[2]/c));
v3_lab[1] = v3_cm[1]/(gamma*(1+beta[2]*v3_cm[2]/c));
v3_lab[2] = (v3_cm[2]+beta[2]*c)/(1+beta[2]*v3_cm[2]/c);
//Fragment 4
v4_lab[0] = v4_cm[0]/(gamma*(1+beta[2]*v3_cm[2]/c));
v4_lab[1] = v4_cm[1]/(gamma*(1+beta[2]*v3_cm[2]/c));
v4_lab[2] = (v4_cm[2]+beta[2]*c)/(1+beta[2]*v3_cm[2]/c);
//Fragment 3
v5_lab[0] = v5_cm[0]/(gamma*(1+beta[2]*v3_cm[2]/c));
v5_lab[1] = v5_cm[1]/(gamma*(1+beta[2]*v3_cm[2]/c));
v5_lab[2] = (v5_cm[2]+beta[2]*c)/(1+beta[2]*v3_cm[2]/c);

```

```
//*****Positions*****
tof1=1500./v1_lab[2];
tof2=1500./v2_lab[2];
tof3=1500./v3_lab[2];
tof4=1500./v4_lab[2];
tof5=1500./v5_lab[2];
//Fragment 1
pos1[0] = v1_lab[0]*tof1;
pos1[1] = v1_lab[1]*tof1;
pos1[2] = v1_lab[2]*tof1;
//Fragment 2
pos2[0] = v2_lab[0]*tof2;
pos2[1] = v2_lab[1]*tof2;
pos2[2] = v2_lab[2]*tof2;
//Fragment 3
pos3[0] = v3_lab[0]*tof3;
pos3[1] = v3_lab[1]*tof3;
pos3[2] = v3_lab[2]*tof3;
//Fragment 4
pos4[0] = v4_lab[0]*tof4;
pos4[1] = v4_lab[1]*tof4;
pos4[2] = v4_lab[2]*tof4;
//Fragment 5
pos5[0] = v5_lab[0]*tof5;
pos5[1] = v5_lab[1]*tof5;
pos5[2] = v5_lab[2]*tof5;
//Filling Histograms
XY_dist.Fill(pos1[0],pos1[1]);
XY_dist.Fill(pos2[0],pos2[1]);
//XY_dist.Fill(pos3[0],pos3[1]);
//XY_dist.Fill(pos4[0],pos4[1]);
//XY_dist.Fill(pos5[0],pos5[1]);
//*****Distances between
fragments*****
//Fragment 1-Fragment 2
dx12 = fabs(pos1[0]-pos2[0]);
dy12 = fabs(pos1[1]-pos2[1]);
//Fragment 1-Fragment 3
dx13 = fabs(pos1[0]-pos3[0]);
dy13 = fabs(pos1[1]-pos3[1]);
//Fragment 1-Fragment 4
dx14 = fabs(pos1[0]-pos4[0]);
```

```
dy14 = fabs(pos1[1]-pos4[1]);
//Fragment 1-Fragment 5
dx15 = fabs(pos1[0]-pos5[0]);
dy15 = fabs(pos1[1]-pos5[1]);
//Fragment 2-Fragment 3
dx23 = fabs(pos2[0]-pos3[0]);
dy23 = fabs(pos2[1]-pos3[1]);
//Fragment 2-Fragment 4
dx24 = fabs(pos2[0]-pos4[0]);
dy24 = fabs(pos2[1]-pos4[1]);
//Fragment 2-Fragment 5
dx25 = fabs(pos2[0]-pos5[0]);
dy25 = fabs(pos2[1]-pos5[1]);
//Fragment 3-Fragment 4
dx34 = fabs(pos3[0]-pos4[0]);
dy34 = fabs(pos3[1]-pos4[1]);
//Fragment 3-Fragment 5
dx35 = fabs(pos3[0]-pos5[0]);
dy35 = fabs(pos3[1]-pos5[1]);
//Fragment 4-Fragment 5
dx45 = fabs(pos4[0]-pos5[0]);
dy45 = fabs(pos4[1]-pos5[1]);
//Double-hit
flag=0;
if(dx12<stripsize && dy12<stripsize){
    dhit12++;
    flag++;
}
if(dx13<stripsize && dy13<stripsize){
    dhit13++;
    flag++;
}
if(dx14<stripsize && dy14<stripsize){
    dhit14++;
    flag++;
}
if(dx15<stripsize && dy15<stripsize){
    dhit15++;
    flag++;
}
if(dx23<stripsize && dy23<stripsize){
    dhit23++;
    flag++;
}
```

```

}
if(dx24<stripsize && dy24<stripsize){
    dhit24++;
    flag++;
}
if(dx25<stripsize && dy25<stripsize){
    dhit25++;
    flag++;
}
if(dx34<stripsize && dy34<stripsize){
    dhit34++;
    flag++;
}
if(dx35<stripsize && dy35<stripsize){
    dhit35++;
    flag++;
}
if(dx45<stripsize && dy45<stripsize){
    dhit45++;
    flag++;
}
//Triple hit
if(flag==3)
    thit++;
//4ple hit
if(flag==4)
    thit++;
//5ple hit
if(flag==5)
    thit++;
cout<<"k="<<k <<flag<<endl;
}
dhit=dhit12+dhit13+dhit14+dhit15+dhit23+dhit24+dhit25+dhit34+dhit35+dhit45;
cout<<"Number of double hits: "<<dhit<< endl;
cout<<"Number of triple hits: "<<thit<< endl;
cout<<"Number of quadruple hits: "<<qhit<< endl;
cout<<"Number of quintuple hits: "<<phit<< endl;
Double_t Prob2=Double_t(dhit)/Double_t(k);
Double_t Prob3=Double_t(thit)/Double_t(k);
Double_t Prob4=Double_t(qhit)/Double_t(k);
Double_t Prob5=Double_t(phit)/Double_t(k);
cout<<"Probability of doublehit: " <<Prob2*100<<"%"<<endl;
cout<<"Probability of triplehit: " <<Prob3*100<<"%"<<endl;

```

```
cout<<"Probability of 4plehit: " <<Prob4*100<<"%"<<endl;
cout<<"Probability of 5plehit: " <<Prob5*100<<"%"<<endl;
cout<<"DONE"<<endl;
```

```
XY_dist.SetMarkerColor(kRed);
//XY_dist.Draw("ZCOL");
//XY_dist.Draw();
}
```



# Agradecimientos

Siempre es difícil escribir una página de agradecimientos, porque cuando la terminas tienes la sensación de que te has olvidado de alguien. De todos modos, intentaré no dejarme a nadie.

En primer lugar querría expresar mi más sincero agradecimiento a mis dos directores, los profesores D. Ignacio Durán Escribano y D. José Benlliure Anaya por darme la oportunidad de unirme a su grupo, por el excelente trato que siempre me han dispensado, así como la paciencia que han mostrado durante la realización de este trabajo.

El segundo agradecimiento es para Héctor Álvarez Pol, porque gracias a su *PIFFIA* y a sus sabios consejos, una parte importante de este estudio ha podido ser llevada a cabo.

Además, quiero dar las gracias a Nolo, a Pablo, a Quique y a todos las personas que han colaborado en la realización de este documento.

Agradezco también a mi familia su apoyo incondicional y mis amigos por los muchos momentos inolvidables.

A todos ellos gracias.

Finally, I would like to express my gratitude to Dr. Klaus Sümmerer and Dr. Yuri Litvinov for their help in the measurements with the scintillators and photomultipliers.



# Bibliography

- [1] [http://www.gsi.de/fair/index\\_e.html](http://www.gsi.de/fair/index_e.html).
- [2] A. Schüttauf. *Nucl. Instr. and Meth. A*, 533:65, 2004.
- [3] T. Suzuki et al. *Phys. Rev. Lett.*, 75:3241, 1995.
- [4] P. Egelhof et al. *Eur. Phys. J. A*, 15:27, 2002.
- [5] M. H. Smedberg et al. *Phys. Lett. B*, 452:1, 1999.
- [6] G. Krein, Th. A. J. Maris, B. B. Rodrigues, and E. A. Veit. *Phys. Rev. C*, 51:2646, 1995.
- [7] T. Aumann, P. F. Bortignon, and H. Emling. *Ann. Rev. Nucl. Part. Sci.*, 48:351, 1998.
- [8] A. Kraznahorkay et al. *Phys. Rev. Lett.*, 82:3216, 1999.
- [9] K.-H. Schmidt et al. *Nucl. Phys. A*, 665:221, 2000.
- [10] J. E. Ducret et al. SPALADIN experiment, performed at GSI, proposal S248.
- [11] H. Müller and B. D. Serot. *Phys. Rev. C*, 52:2072, 1995.
- [12] W. B. Christie et al. *Nucl. Instr. and Meth. A*, 255:466, 1987.
- [13] M. Fernández-Ordóñez. Diploma Thesis, 2002.
- [14] E. Berdermann et al. *Diamond Relat. Mater.*, 10:1770, 2001.
- [15] M. Pfützner et al. *Nucl. Instr. and Meth. B*, 86:213, 1994.
- [16] K.-H. Schmidt et al. *Nucl. Instr. and Meth. A*, 260:287, 1987.
- [17] B. D. Wilkins, E. P. Steinberg, and R. R. Chasman. *Phys. Rev. C*, 14:1832, 1976.

- 
- [18] R. Santonico and R. Cardarelli. *Nucl. Instr. and Meth.*, 187:377, 1981.
- [19] V. V. Parkhomchuck, Pestov Yu. N., and N. V. Petrovykh. *Nucl. Instr. and Meth.*, 93:269, 1971.
- [20] G. F. Knoll. *Radiation Detector and measurement*. John Wiley & sons, New York, second edition, 1989.
- [21] W. R. Leo. *Techniques for Nuclear and Particle Physics experiments*. Springer Verlag, Berlin, Heidelberg, 1987.
- [22] R. Cardarelli, R. Santonico, A. di Biagio, and A. Lucci. *Nucl. Instr. and Meth. A*, 263:20, 1988.
- [23] Y. N. Pestov. *Nucl. Instr. and Meth. A*, 494:447, 2002.
- [24] P Fonte. Applications and new developments in resistive plate chambers, 2001.
- [25] E. Cerron Zeballos et al. *Nucl. Instr. and Meth. A*, 374:132, 1996.
- [26] A. Blanco et al. *Nucl. Instr. and Meth. A*, 485:328, 2002.
- [27] A. N. Akindinov et al. *Nucl. Instr. and Meth. A*, 533:74, 2004.
- [28] Wang Yi et al. *Nucl. Instr. and Meth. A*, 538:425, 2005.
- [29] H. Alvarez Pol et al. *Nucl. Instr. and Meth. A*, 533:79, 2004.
- [30] A. V. Akindinov et al. *Nucl. Instr. and Meth. A*, 533:93, 2004.
- [31] A. V. Akindinov et al. *Nucl. Instr. and Meth. A*, 533:178, 2004.
- [32] F. Anghinolfi et al. *Nucl. Instr. and Meth. A*, 533:183, 2004.
- [33] S. Nishimura et al. *Nucl. Instr. and Meth. A*, 510:377, 2003.
- [34] J. Lu et al. *Nucl. Instr. and Meth. A*, 437:206, 1999.
- [35] Y. Shikaze et al. *Nucl. Instr. and Meth. A*, 455:596, 2000.
- [36] <http://www.ortec-online.com>.
- [37] U. Abbondanno et al. *Nucl. Instr. and Meth. A*, 538:692, 2005.
- [38] <http://www.tektronix.com>.
- [39] <http://fpcongro.usc.es/~hapol/PIFFIA>.

[40] <http://root.cern.ch>.

[41] J. Hoffmann and W. Ott. *GSI Scientific Report*, page 193, 2002.